



# A comprehensive Earth system model (AWI-ESM2.1) with interactive icebergs: effects on surface and deep-ocean characteristics

Lars Ackermann<sup>1</sup>, Thomas Rackow<sup>2,1</sup>, Kai Himstedt<sup>3</sup>, Paul Gierz<sup>1</sup>, Gregor Knorr<sup>1</sup>, and Gerrit Lohmann<sup>1,4</sup>

<sup>1</sup>Alfred-Wegener-Institut, Helmholtz-Zentrum für Polar- und Meeresforschung, Bremerhaven, Germany

<sup>2</sup>European Centre for Medium-Range Weather Forecasts, Bonn, Germany

<sup>3</sup>German Climate Computing Center, Hamburg, Germany

<sup>4</sup>Department of Physics, University of Bremen, Bremen, Germany

**Correspondence:** Lars Ackermann (lars.ackermann@awi.de)

Received: 8 September 2023 – Discussion started: 13 September 2023

Revised: 26 February 2024 – Accepted: 27 February 2024 – Published: 26 April 2024

**Abstract.** The explicit representation of cryospheric components in Earth system models has become more and more important over the last years. However, there are few advanced coupled Earth system models that employ interactive icebergs, and most iceberg model studies focus on iceberg trajectories or ocean surface conditions.

Here, we present multi-centennial simulations with a fully coupled Earth system model including interactive icebergs to assess the effects of heat and freshwater fluxes by iceberg melting on deep-ocean characteristics. The icebergs are modeled as Lagrangian point particles and exchange heat and freshwater fluxes with the ocean. They are seeded in the Southern Ocean, following a realistic present-day size distribution. Total calving fluxes and the locations of discharge are derived from an ice sheet model output which allows for implementation in coupled climate–ice sheet models.

The simulations show a cooling of up to 0.2 K of deep-ocean water masses in all ocean basins that propagates from the southern high latitudes northward. We also find enhanced deep-water formation in the continental shelf area of the Ross Sea, a process commonly underestimated by current climate models. The vertical stratification is weakened by enhanced sea ice formation and duration due to the cooling effect of iceberg melting, leading to a 10 % reduction of the buoyancy frequency in the Ross Sea. The deep-water formation in this region is increased by up to 10 %. By assessing the effects of heat and freshwater fluxes individually, we find latent heat flux to be the main driver of these water mass changes.

The altered freshwater distribution by freshwater fluxes and synergetic effects play only a minor role. Our results emphasize the importance of realistically representing both heat and freshwater fluxes in the high southern latitudes.

## 1 Introduction

Icebergs play a crucial role in Earth's climate system. Their calving from Greenland and the Antarctic continent contributes significantly to the mass balances of the two ice sheets. For Greenland, approximately 550 Gt yr<sup>-1</sup>, representing a third to half of its freshwater release, is due to discharge (Enderlin et al., 2018). For Antarctica, values for iceberg discharge range from over 2000 Gt yr<sup>-1</sup> (Jacobs et al., 1992) to more recent estimates of approximately 1300 Gt yr<sup>-1</sup> (Depporter et al., 2013). Icebergs transport large amounts of fresh water, alter ocean salinity and temperature, and hence affect deep-water and sea ice formation (Grosfeld et al., 2001; Stern et al., 2015). In regions of iceberg melting, the freshwater release leads to a freshening of the upper ocean, increasing the ocean freezing temperature and enhancing stratification. Another direct effect is the cooling of the upper ocean layers by sensible and latent heat fluxes, increasing oceans' density and thus potentially decreasing stratification of the water column, which could counteract the effect of added fresh water. Despite their importance, icebergs are rarely represented in Earth system models (ESMs) in detail,

and if accounted for, their effects on ocean conditions are often only parameterized (Devilliers et al., 2021). Freshwater fluxes from iceberg melting are distributed either homogeneously over a specific area or are treated as surface runoff, entering the ocean directly at coastal regions. The drawbacks of both methods are (1) the neglect of ocean dynamical effects on the icebergs and hence an unrealistic spatial distribution of freshwater release, (2) missing sensible and latent heat feedback from icebergs to the ocean and vice versa, and (3) neglecting iceberg size-dependent dynamics and impacts on the northward extent of the freshwater release and the associated cooling by giant icebergs (Rackow et al., 2017).

Early studies using global ocean models with implemented Lagrangian iceberg models showed a good representation of iceberg trajectories (Bigg et al., 1997; Gladstone et al., 2001). Later studies included interactive icebergs with heat and freshwater feedback into fully coupled ESMs of varying complexity. Jongma et al. (2009) used an Earth system model of intermediate complexity (Claussen et al., 2002). In a simulation with interactive icebergs, they found a decrease in sea ice concentration and associated warming in the Weddell Sea compared to a control run with fresh water homogeneously distributed over the Southern Ocean. Simulations using more advanced models with somewhat higher resolutions of  $1^\circ \times 1^\circ$  for the ocean component were done, e.g., by Martin and Adcroft (2010) and Stern et al. (2016). In comparison to a simulation with iceberg freshwater fluxes parameterized as surface runoff, Martin and Adcroft (2010) found a freshwater export via icebergs from coastal regions resulting in positive salinity anomalies and enhanced deep convection. They also found a decreased sea ice cover. Using a more realistic size distribution, including larger kilometer-scale icebergs, Stern et al. (2016) found a total decrease in sea ice concentration but cooling and freshening of the Weddell Sea. They argue in favor of focusing on large icebergs as these have the most significant effect on temperature and salinity changes. Rackow et al. (2017) add to this point by showing how the inclusion of even larger, giant icebergs impacts the meridional distribution of the iceberg meltwater input in their model simulations. Model simulations with even higher horizontal resolution of about  $0.25^\circ \times 0.25^\circ$  were performed with ocean-only models (Marsh et al., 2015; Merino et al., 2016). They show the importance of icebergs for a realistic representation of Southern Ocean sea ice and its freshwater balance. However, heat fluxes from iceberg fusion were neglected. An overview of coupled climate–iceberg models is given in Table 1.

So far, most studies have focused on surface conditions in the Southern Ocean. However, the effect of interactive icebergs on deep-ocean water masses' characteristics has received less attention due to the necessary long timescales and the associated high computational costs. This question seems especially important concerning the known deep-ocean warm biases in models participating in the Coupled Model Intercomparison Project (CMIP) (Rackow et al.,

2019), which could affect long-term future and paleoclimate simulations, e.g., by their ability to store heat in the abyssal ocean. Warm deep-ocean biases are common among complex Earth system models as found for the Finite-Volume Sea ice-Ocean Model (FESOM) by Sidorenko et al. (2019) and Streffing et al. (2022), as well as other climate models (e.g., Delworth et al., 2006, 2012; Jungclaus et al., 2013; Rackow et al., 2019; Sterl et al., 2012).

This study is the first to investigate the contribution of iceberg freshwater and heat fluxes to deep-ocean properties in a complex Earth system model. We combine a fully coupled ESM with interactive icebergs in the Southern Ocean using a resolution as high as  $\sim 1/3^\circ$  in coastal areas, with a size distribution representing present-day iceberg observations. We use the latest version of the Alfred Wegener Institute Earth System Model (AWI-ESM) with an interactive Lagrangian iceberg model. While the model allows for interactive icebergs in both hemispheres, our simulations only include icebergs in the Southern Ocean. We acknowledge the potential implications of iceberg-related freshwater and heat fluxes for deep-water formation in the North Atlantic and hence on AMOC. However, our primary focus is an enhanced understanding of processes involved in climate–iceberg interactions rather than simulating realistic climatologies.

This study is organized as follows: Sect. 2 describes new developments in the climate and iceberg model as well as the calving mechanism. Furthermore, the simulation setups are summarized. Section 3 analyzes the model results from different simulations with respect to iceberg dynamics and the effects of heat fluxes and the differing freshwater flux distribution, as well as synergetic effects on deep-ocean characteristics. We discuss our results in Sect. 4, and a conclusion is given in Sect. 5.

## 2 Methods and model description

The model used for this study is the AWI Earth System Model (AWI-ESM-2.1) with interactive icebergs. It consists of the AWI Climate Model (Rackow et al., 2018; Sidorenko et al., 2015) but comprises a newer version of the ocean model FESOM. It also uses dynamic vegetation (Reick et al., 2013). Its atmosphere component is the European Centre for Medium-Range Weather Forecasts' Model in Hamburg (ECHAM6) in its sixth generation (Stevens et al., 2013): a general circulation model run with the T63L47 setup, i.e., approximately  $1.9^\circ$  horizontal resolution and 47 layers in the vertical.

ECHAM includes a hydrological discharge model for river runoff (Hagemann and Dümenil, 1997). On a subgrid scale, surface runoff is transported along river routes and released to the ocean domain at the mouth of the river. Runoff is assumed to be liquid. Although a snow layer model is included, snow processes are not considered explicitly in areas that are impermeable to water infiltration, including glacial ar-

**Table 1.** Climate models with interactive iceberg component and freshwater feedback. *Model* gives the model name. If ocean components differ between model versions, it is indicated by brackets. *Hor. resolution* and *vert. levels* give the horizontal resolution and number of vertical levels; *HF cpl.* states whether heat flux feedback from iceberg melting is included. *Seeding* states the size distribution used. For the Southern Hemisphere, the following are used: GL – Gladstone et al. (2001), TO – Tournadre et al. (2016). For the Northern Hemisphere the following are used: BI – Bigg et al. (1996), Dowdeswell et al. (1992). *Run length* gives the integration time of the simulations.

Model	Hor. resolution/ vert. levels	HF cpl.	Seeding	Run length [yr]	References
ECBilt-CLIO*	3°/20	yes	GL	100 <sup>1</sup>	Jongma et al. (2009)
GFDL CM2G (GOLD)	1°/63	yes	GL	120	Martin and Adcroft (2010)
GFDL CM2G (MOM6)	1°/63	yes	TO	120	Stern et al. (2016)
iLOVECLIM*	3°/20	yes	BI**	12 000	Bügelmayer et al. (2015)
LOVECLIM*	3°/20	yes	uniformly**	future scenarios	Schloesser et al. (2019)
NEMO-ICB	0.25°/75	no <sup>2</sup>	GL	20/30	Marsh et al. (2015); Merino et al. (2016)
UKESM	1°/75	– <sup>3</sup>	GL**	45 + future scenario	Siahaan et al. (2022); Smith et al. (2021)

<sup>1</sup> Jongma et al. (2009) used a 900-year spin-up. <sup>2</sup> Marsh et al. (2015) state that heat flux feedback is implemented but turned off. <sup>3</sup> UKESM uses NEMO-ICB as the ocean model and hence allows for heat flux feedback; however, no statement is given whether it is turned on or off. \* The model is of intermediate complexity (EMIC). \*\* Total discharge is given by an interactive ice sheet model.

eas (Reick et al., 2021). Here, excess precipitation, including snowfall, is just added to the surface runoff as liquid fresh water. However, latent heat fluxes only include evaporation and sublimation according to the atmospheric water vapor. Hence, the river discharge implicitly accounts for the mass balance of glaciers, including freshwater fluxes from iceberg discharge and basal melting. But latent heat fluxes from iceberg melting are not accounted for. A detailed description of the land surface and hydrological discharge components can be found in (Reick et al., 2021).

The ocean model used here is version 2 of FESOM, the Finite-VolumE Sea ice-Ocean Model (FESOM2). In contrast to its predecessor (Wang et al., 2014), it now employs the finite-volume method instead of finite elements, which allows for higher computational efficiency (Danilov et al., 2017). The model uses unstructured meshes that enable efficient high-resolution modeling of highly dynamic regions while leaving a coarser resolution in other regions. The mesh used in this study shows a horizontal resolution of up to 20 km in the high-latitude coastal regions and a coarser resolution of around 120 km in the low latitudes. It has been widely used (e.g., Danabasoglu et al., 2016; Sein et al., 2016; Wang et al., 2016a, b) and is applicable for long-term simulations. The iceberg component runs as a submodel of the ocean–sea ice model FESOM2 (Danilov et al., 2017; Koldunov et al., 2019; Scholz et al., 2019, 2022). In contrast to a previous version of this model introduced by Rackow et al. (2017), freshwater and heat fluxes are now interactive, providing a new level of coupled feedbacks. The initial position, number, and proportions of icebergs are derived from an ice sheet model (ISM) output, allowing future applications in a coupled climate–ice sheet setup. The iceberg size distribution follows a  $-3/2$  power law, derived from satellite observations for both open-ocean and near-coastal areas (Barbat et al., 2019; Tournadre et al., 2016).

## 2.1 The iceberg module

The iceberg component is a submodel of FESOM. However, bidirectional coupling between the ocean and the iceberg had yet to be implemented in the model. Studies using the interactive iceberg component were ocean-only simulations, in which the icebergs were treated as passive tracers that allowed diagnosing a meltwater field (Rackow et al., 2017), lacking freshwater and heat feedback to the ocean model. This work introduces the iceberg module as a fully coupled component within FESOM. Hence, freshwater and heat fluxes are bidirectionally coupled between icebergs and the ocean.

Initial iceberg positions and dimensions are obtained via fields of calving discharge from the ice sheet (see Sect. 2.2 for details). The model is a Lagrangian iceberg model; i.e., all icebergs are represented by point particles. While these particles are zero-dimensional, each has a length, width, and height assigned to it. These physical quantities are altered during the simulation by thermodynamical processes. For simplification, each iceberg is assumed to have a quadratic base area and to be of cuboidal shape. Thermodynamics take into account the erosion by surface waves and buoyant convection mainly following work by Bigg et al. (1997), Gladstone et al. (2001), and Martin and Adcroft (2010), as well as basal and lateral “basal” melting following the three-equation formulation by Hellmer and Olbers (1989) and Holland and Jenkins (1999). Lateral basal melting here refers to melting on the submerged sides of an iceberg by turbulent heat transfer analogously to the melting at the base of an iceberg. It is not to be confused with buoyant convection. The implementation is motivated by Bigg et al. (1997) and is described in Rackow et al. (2017). The wave erosion follows an empirical formulation, taking into account the sea surface temperature, the relative velocity between wind and

ocean, and a damping factor that is a function of sea ice cover. The buoyant convection also follows an empirical formulation and depends on the “thermal driving” temperature  $T_d = \max(0, T_m - T_f)$ , with  $T_f$  being the in situ freezing temperature at mid-depth and  $T_m$  being the average water temperature along the iceberg draft. The basal (and lateral basal) melt rates are derived by solving the energy and salinity balances in the boundary layer at the iceberg–ocean interface given far-field temperature and salinity values. For the basal melting, temperature and salinity at iceberg depth are taken, and for the lateral basal melting, temperature and salinity are averaged along the iceberg depth. This approach allows for negative melt rates, i.e., freezing at the iceberg base. Besides accounting for the wind drag, no exchange processes with the atmosphere are modeled, particularly no surface mass balance and radiative or conductive heat fluxes. The surface melt due to radiation is of minor importance compared to oceanic-driven melt rates (Bigg et al., 1997). A detailed description of the model can be found in Rackow (2011) and Rackow et al. (2017). Interactions between icebergs are not modeled but are parameterized in a very simple manner to avoid an overloading of ocean cells: if an iceberg is about to change from one grid element to another, the total iceberg area contained in this grid element is summed up. If the new iceberg leads to a larger total iceberg area than the actual element area, it does not change the grid element but stays in its previous grid element and is set back to its previous position. It can still move within the grid cell element or to a neighboring grid cell that is not saturated yet. Furthermore, model icebergs are not discharged into saturated ocean grid cells but are distributed over the coastal and neighboring grid cells within the respective basin (Fig. 1). Whenever the model iceberg’s depth reaches deeper than the local bathymetry, it is assumed to be grounded, and its velocity is set to zero. Basal melting can still occur and eventually set the model iceberg free again once its depth is sufficiently reduced.

Different measures have been taken to speed up the iceberg module: the first is by implementing a “scaling approach” similar to Martin and Adcroft (2010). This approach reduces the number of simulated icebergs by dividing the icebergs into different size classes. For each class, a scaling factor is defined by which the number of simulated icebergs is reduced. Each simulated iceberg then represents multiple other icebergs. The calculated freshwater and heat fluxes are multiplied by the scaling factor to ensure mass and energy conservation (Appendix A). A second approach for speeding up the iceberg module is a variable coupling frequency between ocean and iceberg components. Initially, the coupling and, hence, the simulation of icebergs took place every FESOM ocean time step. Due to the relatively slow movements of the icebergs, a coupling three or four times a simulated day seems to be sufficient instead of the one-to-one coupling implemented previously.

Freshwater and heat fluxes from iceberg melting are added to the respective FESOM internal sea ice fluxes. Hence, the

iceberg feedback is applied to the ocean surface. Furthermore, it is distributed to all nodes that constitute the containing element. The calving discharge is compensated for by a reduction of Antarctic surface runoff. As the calving flux is considered constant in our simulation setup, the surface runoff reduction is also considered constant and is done at every coupling time step between the atmosphere (land surface) and the ocean. The total salinity is held constant in FESOM internally, and local surface freshwater fluxes (like those from iceberg melting in our model setup) are balanced by a freshwater compensation distributed homogeneously over the whole ocean domain. Hence, both fluxes together, the iceberg melting and the reduced surface runoff, lead to a redistribution of fresh water from the coastline to the open ocean. While there is temporal variability in the iceberg melt fluxes, the compensating reduction of Antarctica’s surface runoff is fixed over time. To account for this discrepancy and to ensure a consistent freshwater budget, the total salinity is balanced, so the iceberg setup has no additional net freshwater flux compared to the model version without interactive icebergs. However, the freshwater fluxes from iceberg melting are not considered part of the Antarctic surface runoff anymore; i.e., the influx is allowed to occur on the open ocean instead of directly along the coast and shelf regions. While the total salinity is balanced, oceans’ total internal energy is not, and there is a negative net heat flux due to iceberg melting that is not accounted for in the model setup without interactive icebergs. Hence, a new climatological equilibrium is expected to develop compared to the default model setup without interactive icebergs.

## 2.2 Iceberg seeding and experimental setup

The initial conditions of each iceberg need to be provided, including the location, velocity, dimensions, and scaling factors. Apart from the velocities, which are set to zero initially, all other parameters are deduced from the ice sheet model output. For our study, this is the Parallel Ice Sheet Model (PISM) (Martin et al., 2011; Winkelmann et al., 2011). The model output provides a spatially continuous calving and discharge field on a  $16 \times 16$  km grid (Fig. 1) with the highest calving rates per grid cell of up to  $10 \text{ Gt yr}^{-1}$  (approximately  $45 \text{ m yr}^{-1}$ ) along the Filchner–Ronne and the Ross ice shelves as well as in the Amundsen Sea, which corresponds to with observations (Depoorter et al., 2013).

To generate discrete icebergs from the continuous field, the calving flux is summed up over each basin (Fig. 1a) to get the integrated total amount of ice discharge within each basin. Next, this amount is divided by a reference iceberg height of 250 m to get a total calving area. As a reference iceberg size to derive the total number of seeded icebergs, the median of the power-law distribution is used. Following Tournadre et al. (2016), individual iceberg areas are drawn from a power-law distribution. The initial size distribution is shown in Fig. 1b, with the vast majority of icebergs being



rather small ( $0.01\text{--}1\text{ km}^2$ ) and only a few being larger than  $100\text{ km}^2$ . A maximum iceberg area of  $400\text{ km}^2$  is assumed to avoid iceberg areas being larger than an ocean grid cell. Model icebergs are assumed to have a quadratic surface. The iceberg height is set to be equal to the length and width, but not larger than 250 m. This new feature compared to the previous iceberg model version (in which iceberg height was set to 250 m) is implemented to reduce the risk of instantaneous grounding of newly seeded icebergs in shallow-water regions. In an iterative process, the dimensions are adjusted so that the total iceberg volume matches the integrated discharge. An overview of this scheme is given in Fig. A1.

For each size class (Fig. 1b), a specific scaling value is set by which the number of icebergs in this size class is reduced (Table A). The heat and freshwater fluxes released by this iceberg are then scaled up again accordingly. For the seeding, a list of ocean grid cells is generated. For each ice sheet model grid cell in which calving occurs, the nearest ocean grid cell and the neighboring cells are added to this list. Direct coastal grid cells are then removed from this list to reduce the risk of instantaneous grounding. So, model icebergs are spread out near the coast but are not seeded directly at the coast. For each basin, model icebergs are then distributed over the ocean grid cells contained in the list. These steps are done for each basin individually to ensure a consistent distribution along the coastline. While the same size distribution is applied for each basin, the actual model icebergs are drawn randomly from this particular distribution. Hence, the actual size distribution may vary for each grid point. The total calving flux of roughly  $1731\text{ Gt yr}^{-1}$  is subtracted from the surface runoff to ensure a closed water balance (Fig. 1c).

To spin up the iceberg model, an equilibrated pre-industrial run has been continued with icebergs but with freshwater and heat feedback turned off ( $\text{ICB}_{\text{spinup}}$ ). This spin-up was run for 100 years, after which the total iceberg melt flux balances the calving flux (Fig. 1c). Several experiments were branched off from this spin-up: a fully coupled run with icebergs (ICB), two partially coupled iceberg runs, one without latent heat fluxes from iceberg fusion ( $\text{ICB}_{\text{FW}}$ ), and one without iceberg meltwater feedback ( $\text{ICB}_{\text{HF}}$ ). The same iceberg setup has been used for these runs. Additionally, a control run without icebergs (CTL) has been run. All runs are summarized in Table 2.

### 3 Results

This section presents the results of a pre-industrial run with interactive icebergs as well as only partially coupled runs with either freshwater or heat flux feedback, each running for 700 years. The results presented are averaged over the last hundred model years of the simulations. Temperature and salinity fields of CTL with respect to the Polar Science Center Hydrographic Climatology (PHC3.0) (Steele et al., 2001) are shown in Fig. 2. Strong warm biases in the deep Southern

Ocean of up to  $1\text{--}2\text{ K}$  are present in CTL, most pronounced in the Atlantic and Indian Ocean sectors (Fig. 2a–c). Furthermore, there is a pronounced fresh bias in the continental shelf regions around Antarctica of up to 0.5 psu (Fig. 2d–f). Deep-ocean conditions of CTL and ICB with respect to (PHC3.0) (Steele et al., 2001) are shown in Figs. A2 and A3.

#### 3.1 Trajectories

Figure 3a illustrates iceberg trajectories for the fully coupled iceberg run ICB. Two main pathways can be recognized: one branching off the Antarctic Peninsula, where small and large icebergs follow the Antarctic Circumpolar Current (ACC), and one pathway in the Ross Sea with medium-sized icebergs. A third branch of icebergs, escaping the ACC near the Kerguelen Plateau as recognizable in the observational data (Fig. 3d) and found by Rackow et al. (2017), is not present in our model results. Large icebergs tend to stay along the coast, following the Antarctic Coastal Current. The general patterns resemble satellite observations for giant icebergs by Budge and Long (2018) and Stuart and Long (2011) (Fig. 3d). However, model icebergs travel further north compared to observations. In the Ross Sea, their pathways are confined by the Antarctic Convergence Zone (indicated as the zone between the  $2$  and  $5\text{ }^\circ\text{C}$  SST isotherms). The spatial patterns of freshwater and heat fluxes (Fig. 3b and c) match the trajectories and show melting hot spots near the coast, inside the Weddell Sea, and at the tip of the Antarctic peninsula where, very locally, freshwater and heat fluxes of over  $10\text{ m yr}^{-1}$  and  $10\text{ W m}^{-2}$ , respectively, are reached.

#### 3.2 Surface conditions

The anomalies for sea surface salinity (SSS), sea surface temperature (SST), and sea ice height are shown in Fig. 4 for ICB,  $\text{ICB}_{\text{HF}}$ ,  $\text{ICB}_{\text{FW}}$ , and CTL with respect to the spin-up. ICB,  $\text{ICB}_{\text{HF}}$ , and  $\text{ICB}_{\text{FW}}$  show pronounced positive salinity anomalies in the shelf regions of the Weddell Sea (Fig. 4a and g). A similar salinity anomaly is detected in the Ross Sea sector in  $\text{ICB}_{\text{HF}}$ . However, the underlying dynamics are fundamentally different. In ICB and  $\text{ICB}_{\text{FW}}$ , the surface runoff is the most reduced compared to CTL in areas that correspond to the coastal regions with the highest calving rates. In these areas, fresh water by iceberg calving is parameterized via the river-routing scheme and eventually treated as river discharge in CTL and  $\text{ICB}_{\text{HF}}$ . As the icebergs do not melt entirely in their regions of origin but rather further north off the coast, the model experiences a relative freshwater export from near-coast shelf regions, which results in pronounced positive salinity anomalies in the shelf regions of the Weddell Sea in ICB and  $\text{ICB}_{\text{FW}}$ . In contrast, in  $\text{ICB}_{\text{HF}}$  (in which the surface runoff is not altered compared to CTL), enhanced sea ice formation (Fig. 4i) leads to increased brine rejection. This can be recognized in the Weddell Sea shelf region and the Ross Sea. These regions of positive salinity anomaly

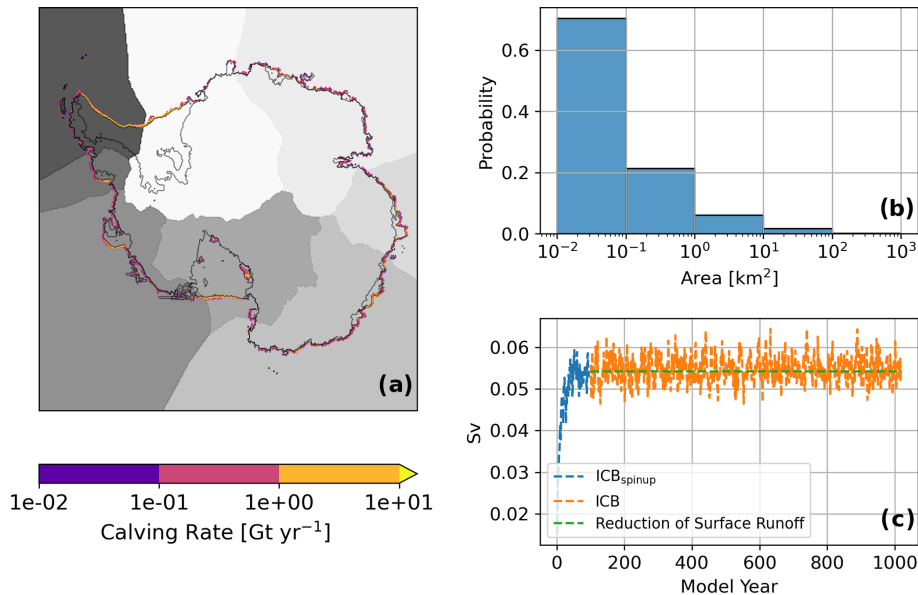


**Figure 1.** (a) Calving flux from a PISM stand-alone simulation. The gray-shaded areas depict different basins for which the integrated total discharge is calculated individually. (b) Size distribution of seeded icebergs. (c) Iceberg-related freshwater flux for spin-up and ICB, as well as the reduction of Antarctica's surface runoff.

**Table 2.** Experiments run within the scope of this study. *Exp. ID* indicates the name used for this experiment throughout this study. *FW* and *HF* indicate how freshwater and heat fluxes from iceberg melting are treated within the simulation. *Scaling* indicates that the scaling approach mentioned in Sect. 2.1 is applied. *Cpl. frequency* indicates the coupling frequency in FESOM time steps per iceberg submodel time step. *Run length* indicates the length of the simulation in model years.

Exp. ID	FW	HF	Scaling	Cpl. frequency [-]	Run length [yr]
ICB <sub>spinup</sub>	surface runoff	absent	yes	8	100
CTL	surface runoff	absent	–	–	700
ICB	interactive	interactive	yes	8	700
ICB <sub>FW</sub>	interactive	absent	yes	8	700
ICB <sub>HF</sub>	surface runoff	interactive	yes	8	700

match the pattern of increased sea ice height well for ICB<sub>HF</sub> (Fig. 4g and i). Increased sea ice cover in ICB and ICB<sub>HF</sub> is very pronounced at the end of the summer season on the shelf regions (Fig. A4) and along the sea ice edge at the end of the winter season (Fig. A5). In contrast, no systematic increase in sea ice height can be recognized in this region in ICB and ICB<sub>FW</sub> (Fig. 4c and f). Here, the increased salinity due to reduced near-coastal freshwater surface runoff inhibits additional sea ice growth. But sea ice growth is fostered in coastal regions of the Amundsen and Bellingshausen seas, along the Antarctic Peninsula, and along the Wilkes Land coast (Fig. 4c). Here, freshwater and heat fluxes from iceberg melting are very high (Fig. 3b and c). Cooling patterns can be seen in the Weddell Sea and the Indian sector of the Southern Ocean (Fig. 4b and h), while warming is detected in the Amundsen and Bellingshausen seas, as well as in the Ross Sea, leading to a dipole of warm–cold anomalies across

the Antarctic Peninsula. The warming in the Amundsen and Bellingshausen seas is linked to an increase in surface salinity that leads to enhanced vertical mixing and upward mixing of heat. In contrast to the similar cooling patterns in ICB and ICB<sub>HF</sub>, a warming in the Weddell Sea can be recognized in ICB<sub>FW</sub> (Fig. 4e). In this experiment, an increase in salinity also leads to enhanced vertical mixing and convective mixing of heat as in ICB and ICB<sub>HF</sub>, but latent cooling from iceberg melting is missing to compensate for this surface warming. In general, the resulting responses for SST, SSS, and sea ice height are dominated by the individual effects of heat and freshwater fluxes in ICB, revealing minor importance of synergistic effects on long timescales.

To assess atmospheric feedbacks, the mean zonal wind anomaly and the contributions to Antarctica's mass balance are shown in Figs. A6 and A7, respectively. A weakening of the westerlies south of 40° S of less than 10 % can be seen

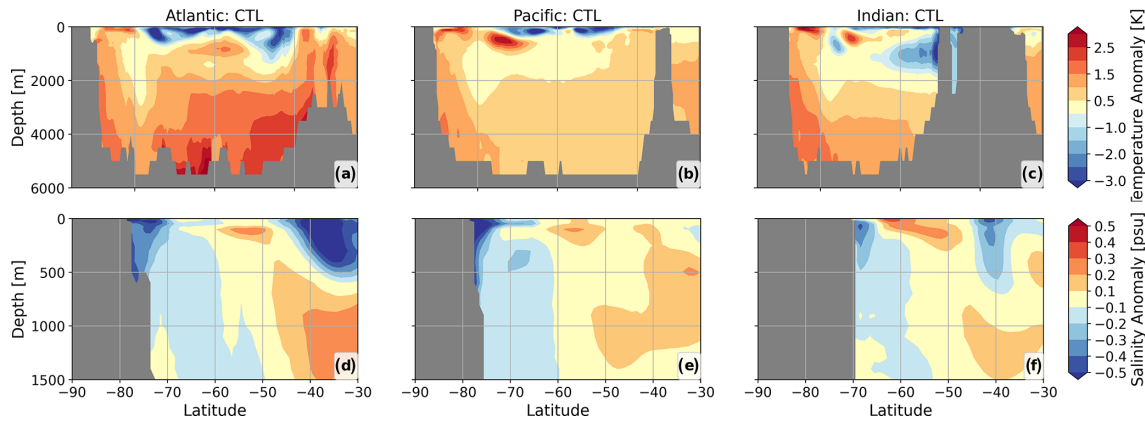


**Figure 2.** (a–c) Zonal mean temperature anomaly for the Atlantic, Pacific, and Indian Ocean sectors, respectively, of CTL with respect to PHC3.0 (Steele et al., 2001). Panels (d)–(f) are like (a)–(c) but for salinity and limited to the upper 1500 m and 30–90° S.

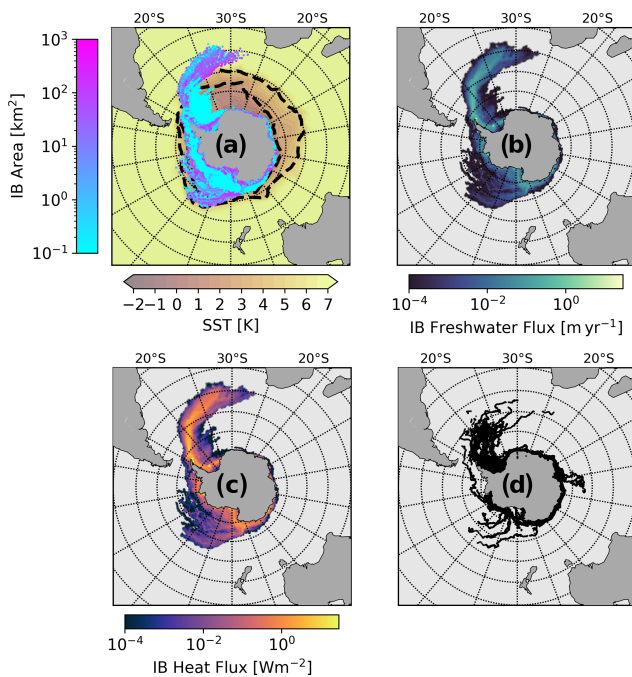


**Figure 3.** (a) Sea surface temperature (SST) overlaid by iceberg trajectories with iceberg surface area shown on a logarithmic color bar. The black dashed contour lines indicate the Antarctic Convergence Zone where SST falls from 5 to 2 °C. (b) Freshwater flux due to iceberg melting; (c) heat flux due to iceberg melting. (d) Satellite observations from the QuikSCAT portion of the Antarctic Iceberg Tracking Database (Budge and Long, 2018; Stuart and Long, 2011) over the period from 1991 to 2022. All model results are averaged over model years 600–700.

in ICB compared to CTL. Regarding Antarctica’s mass balance, the discharge (freshwater runoff via the river-routing scheme) is reduced by 1731 Gt yr<sup>-1</sup> in ICB and ICB<sub>FW</sub> as mentioned in Sect. 2.1 (Fig. A7a). Changes in P–E and glacial melt are insignificant (Fig. A7b and c).

### 3.3 Deep-ocean conditions

Changes in deep-ocean temperature for the Atlantic, Pacific, and Indian Ocean basins are illustrated in Fig. 5. After 700 model years, a cooling in all three basins can be seen for ICB and ICB<sub>HF</sub> with respect to the spin-up run. The cooling of up to –0.2 K is most pronounced in the Pacific (Fig. 5b and h). While no cooling is recognizable in ICB<sub>FW</sub>, the patterns of ICB and ICB<sub>HF</sub> look very similar. The cooling signal extends from the surface layers of the Southern Ocean’s Atlantic section (Fig. 5a and g) to the deep southern mid-latitudes. A cold cell can be seen in the North Atlantic at around 1000 m depth. The deep North Atlantic and the Arctic Ocean show a warming trend. However, this is partly due to a general background trend and internal model variability as it is also visible for the control run (Fig. 5j). In contrast to the Atlantic basin, the cooling in the Pacific Ocean and Indian Ocean extends over the whole basins (Fig. 5b, c, h, and i). Most pronounced in the Southern Ocean, it spreads more northward with depth. However, the upper ocean layers show a warming in the high-latitude Pacific section of the Southern Ocean, corresponding to the warming of the Ross Sea (Fig. 4a, d, g). This effect is also visible in ICB<sub>FW</sub>. Also here, CTL shows a slight warming (Fig. 5k) but with a much smaller magnitude than the other simulations.

A strong increase in salinity can be seen in ICB and ICB<sub>HF</sub> in the Atlantic and Pacific sectors from the surface to a depth of around 500 m (Fig. 6a, b and g, h). These salinity anomalies are mainly detected in the shelf regions of the Weddell and Ross seas, indicating a link to the surface conditions (SSS anomalies in Fig. 4). However, ICB<sub>FW</sub> also shows pos-

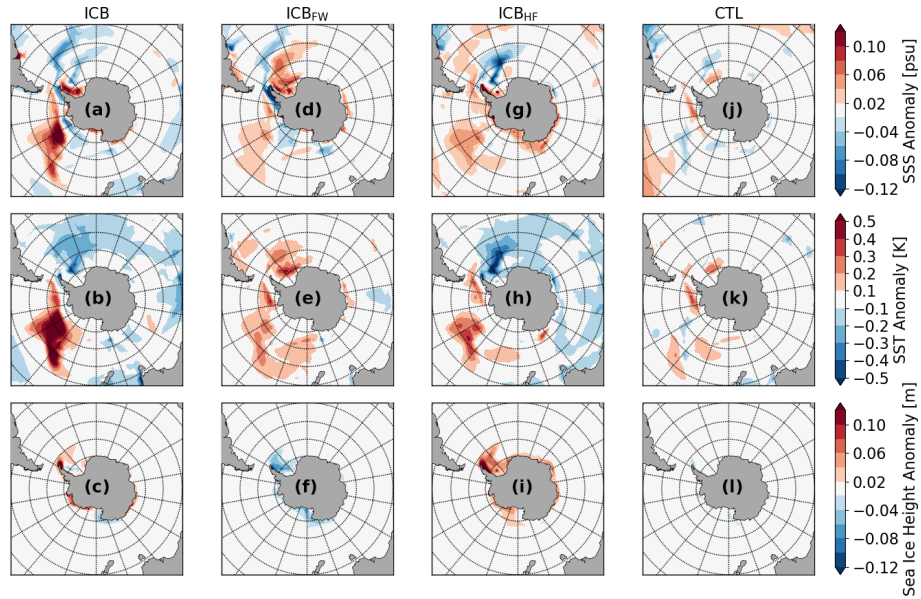


**Figure 4.** Multiyear anomalies of SSS, SST, and sea ice height for the experiments ICB (a–c), ICB<sub>FW</sub> (d–f), ICB<sub>HF</sub> (g–i), and CTL (j–l). All results are averaged over model years 600–700 and anomalies are calculated with respect to the spin-up.

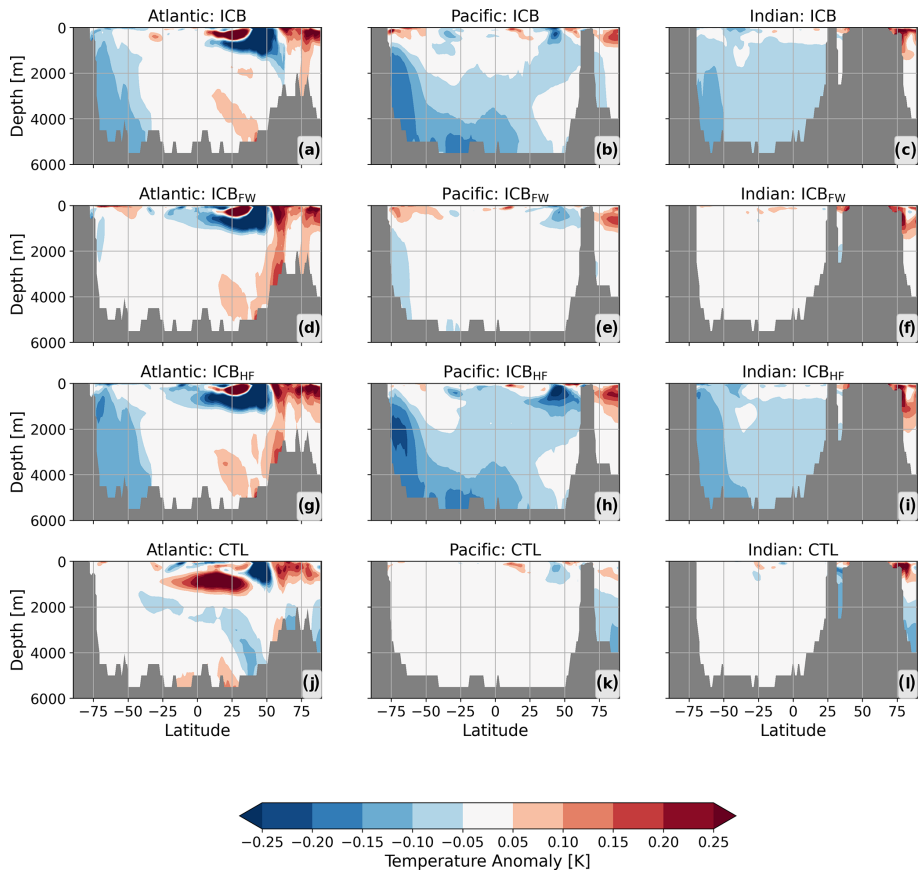


**Figure 5.** (a–c) Temperature anomalies for the Atlantic, Pacific, and Indian Ocean, respectively, for ICB. (d–f) Temperature anomalies for ICB<sub>FW</sub>. (g–i) Temperature anomalies for ICB<sub>HF</sub>. (j–l) Temperature anomalies for CTL. All results are averaged over model years 600–700 and anomalies are calculated with respect to the spin-up.

itive SSS anomalies, especially in the Weddell Sea, but the vertical extension is limited to mixed layer depths (Fig. 6d). The main driver for the positive salinity anomalies reaching deeper levels is therefore attributed to the latent heat flux from iceberg melting. The effect of altered spatial freshwater distribution, on the other hand, plays a minor role.

### 3.4 Impact of HF and FW on adjustment timescales

The effect of temperature changes on seawater density is small compared to the effects of salinity in our experiments. The salinity increase leads to a positive density anomaly and, hence, to a weakening of vertical stratification. This weakening is especially pronounced over the continental shelf in the Ross Sea in ICB and ICB<sub>HF</sub> and additionally along the coast of Wilkes Land in ICB<sub>HF</sub> (Fig. 7). ICB<sub>FW</sub> shows a strengthening of stratification around Antarctica except for the Weddell Sea. The change in the buoyancy frequency affects the magnitude of vertical mixing (Fig. A9) that is reduced (enhanced) in the Weddell Sea for ICB<sub>HF</sub> and ICB (CTL and ICB<sub>FW</sub>). The increased vertical mixing in the open-ocean part of the Amundsen seas in ICB leads to an upward heat transport that results in surface warming (Fig. 4a).

This weakened vertical stratification in the Southern Ocean results in enhanced deep convection over continental shelves and enhanced formation of Antarctic Bottom Water (AABW) (Fig. 8). The AABW in the Indo-Pacific sector (AABW-IP) is increased by up to 10 % in ICB and ICB<sub>HF</sub>, though this change lies within 1 standard deviation. The AABW-IP strengthening occurs within the first 200 model years and stays at a rather constant level afterward. ICB<sub>FW</sub> and CTL show a weak trend. All simulations show a pronounced centennial variability in the AABW, indicating that this feature is due to internal model variability. As changes in AABW formation in the Atlantic sector only represent a minor contribution, global AABW mainly follows the AABW-IP signature originating in the Ross Sea shelf region as the main area, which is affected by destabilized stratification due to iceberg heat fluxes. The global ocean temperature decreases by approximately 0.01 K per century over the first 400 years in ICB and ICB<sub>HF</sub>. This corresponds to a rough calculation considering the enthalpy of fusion for a discharge flux of around 1700 Gt yr<sup>-1</sup> (Appendix). After 400 years, the cooling trend in ICB flattens, while it continues to decrease in ICB<sub>HF</sub>. The altered freshwater distribution via iceberg transport hence buffers the cooling. No cooling trend is recognizable in CTL and ICB<sub>FW</sub>. The Drake Passage throughflow is around 87–90 Sv in CTL, which is significantly smaller than suggested by observations (Donohue et al., 2016; Whitworth and Peterson, 1985). In our simulations, the Drake Passage throughflow increases to around 92 Sv in ICB. However, this increase lies within 1 standard deviation. The Weddell Gyre strength shows similar variability and amplitude (80–89 Sv) for all simulations, and no clear differences between ICB

and CTL can be seen. For comparison, the barotropic stream function is shown in Fig. A8.

## 4 Discussion

We have run multi-centennial simulations with a complex fully coupled Earth system model, including interactive icebergs. While the iceberg trajectories show generally good agreement with observations, there are also some discrepancies. There are no icebergs branching off near the Kerguelen Plateau in our simulations as seen in observations (Fig. 3) or as found by Rackow et al. (2017) in their ocean-only simulations with prescribed atmospheric forcing. This might be due to the coarse resolution of the atmosphere and land surface. Steep orographic gradients are smoothed out, which hinders the formation of katabatic winds. Instead, icebergs are mainly affected by polar easterlies and hence pushed onshore due to Ekman dynamics. Another reason could be that the threshold values for the “sea ice capturing mechanism” might need to be lowered or tuned after the switch from FESOM1 to FESOM2. In the earlier version, a sea ice strength of at least  $P_s = 10000 \text{ Nm}^{-1}$  was assumed to allow this mechanism, and modeled sea ice strength in this area might be smaller in FESOM2. Rackow et al. (2017) noted that the two largest giant icebergs in their simulation left the coastal current near the Kerguelen Plateau only because of being captured by the expanding sea ice and thus being able to cross the southern ACC front (Orsi et al., 1995), which would be difficult just via the other model dynamics due to the tendency of giant icebergs to follow isolines of SSH. In general, large model icebergs tend to be too confined to coastal regions. This was already found by Rackow et al. (2017) and other studies (e.g., Merino et al., 2016). When being able to leave the coast, the icebergs show a drift further north in our simulations than in observations but do not travel distances as long as in Rackow et al. (2017). However, the observational data used here only covers icebergs larger than  $\sim 5\text{--}6$  km (Stuart and Long, 2011) and hence can miss substantial parts of the end of giant icebergs’ trajectories. The iceberg model, on the other hand, does not include a breakup parameterization for large icebergs. Hence, the occurrence and longevity of large icebergs might be overestimated when compared to observations. As the dynamics of small and large icebergs differ (Rackow et al., 2017), a breakup parameterization would affect trajectories and melt patterns (England et al., 2020). The simple parameterization implemented in our model to avoid an overfilling of ocean grid cells leads to very long residence times of icebergs. Icebergs tend to accumulate in certain places, e.g., the tip of the Antarctic Peninsula (Fig. 3). They may block the pathway for more downstream icebergs when a grid cell is saturated, although other model icebergs are not taken into account in one single iceberg’s momentum balance. The long residence times delay the escape to open-ocean waters where

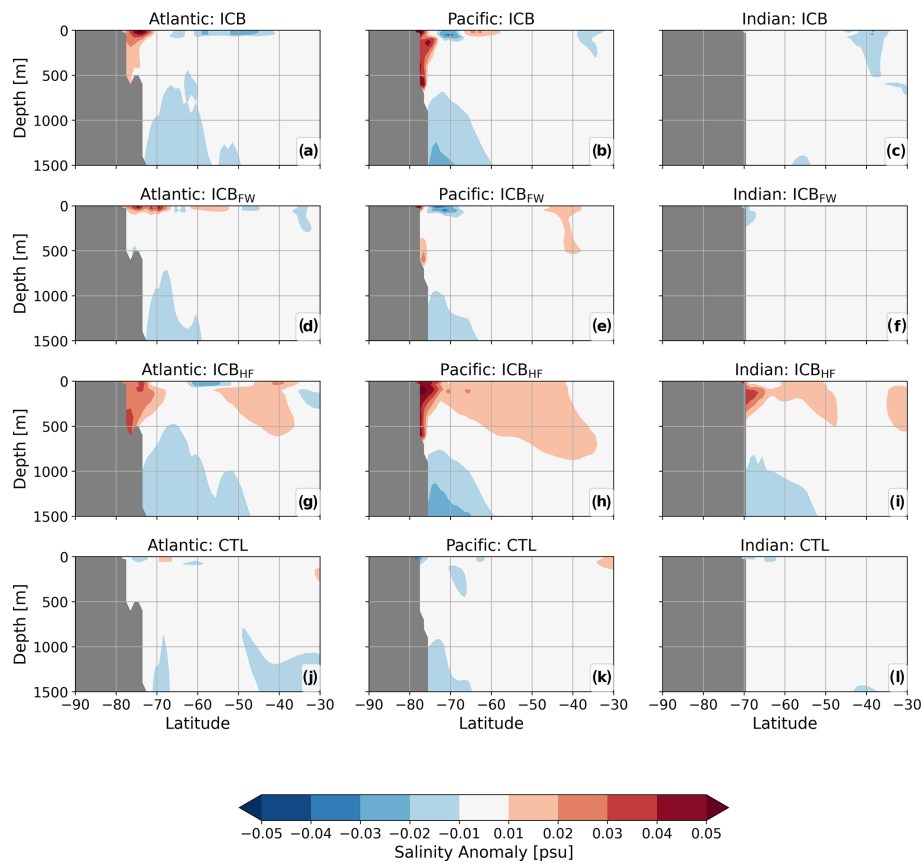


**Figure 6.** (a–c) Salinity anomalies for the upper 1500 m of the Atlantic, Pacific, and Indian Ocean sections of the Southern Ocean for ICB. (d–f) Salinity anomalies for ICB<sub>FW</sub>. (g–i) Salinity anomalies for ICB<sub>HF</sub>. (j–l) Salinity anomalies for CTL. All results are averaged over model years 600–700 and anomalies are calculated with respect to the spin-up.

a breakup parameterization, like the “footloose” mechanism used in England et al. (2020), would come into play. In this way, large icebergs decay predominantly near the coast, and long trajectories, as mentioned in Rackow et al. (2017), are avoided.

Physical feedbacks besides freshwater and heat fluxes are not represented in the iceberg model. These feedbacks may include effects on surface albedo, surface wind stress, and sea surface height. Furthermore, we used a uniform calving size distribution for all ocean basins. However, size distributions vary at different locations, and giant icebergs calve very rarely (Qi et al., 2021). Hence, they should be treated as statistically rare events similar to volcanic eruptions, for example, by calving them stochastically in ensemble simulations or by prescribing their time-mean effects via pre-computed melt climatologies (Stern et al., 2016; Rackow et al., 2017).

The effects on sea surface conditions support the findings of previous studies. Martin and Adcroft (2010) and Stern et al. (2016) also found warming in the Amundsen and Bellingshausen seas as well as in the Ross Sea. This warming is explained by increased upward heat transport due to a destabilization of the upper ocean layer’s stratification. This

weakened stratification stems from increased salinity due to northward freshwater export. The warming in the open-ocean part of the Amundsen Sea (Fig. 4b) is consistent with findings by Martin and Adcroft (2010). In our simulations, this warming is most pronounced in the upper 100 m. The time series of this warm anomaly averaged between 110–130° W and 55–65° S shows a strong multi-centennial variability (Fig. A7d) and a consistent warming in ICB compared to CTL. However, the mechanism behind this pattern may be more complex as the warming occurs far off the coast and off iceberg trajectories (Fig. 3a), and no significant correlations with the Weddell Gyre strength ( $r = -0.20$ ), the Drake Passage throughflow ( $r = -0.12$ ), or the Southern Annular Mode (SAM) ( $r = -0.20$ ) (Fig. A7e) are found.

In our ICB and ICB<sub>FW</sub> experiments, the surface runoff is reduced by the amount of iceberg discharge. This leads to positive salinity anomalies in the Weddell Sea (especially pronounced in the Weddell Sea shelf region) and the Ross Sea shelf region (Fig. 4a and d). However, our simulation ICB<sub>HF</sub> also shows a strong increase in salinity despite unaltered surface runoff. Hence, increased sea ice formation and duration also play an important role in Ross Sea’s freshwater



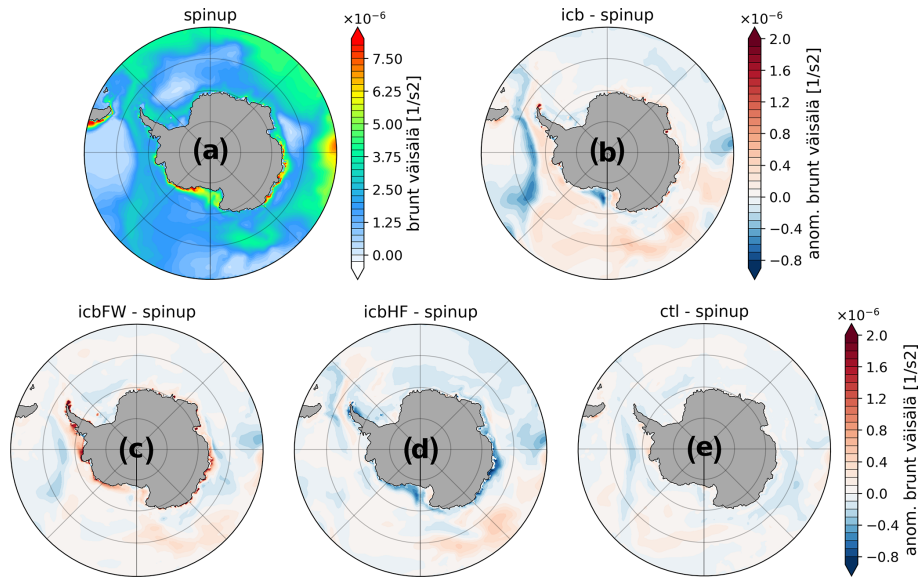


**Figure 7.** Brunt–Väisälä frequency for spin-up (a) and anomalies for ICB (b), ICB<sub>HF</sub> (c), ICB<sub>FW</sub> (d), and CTL (e) with respect to spin-up averaged over the upper 250 m and for the model years 600–700.

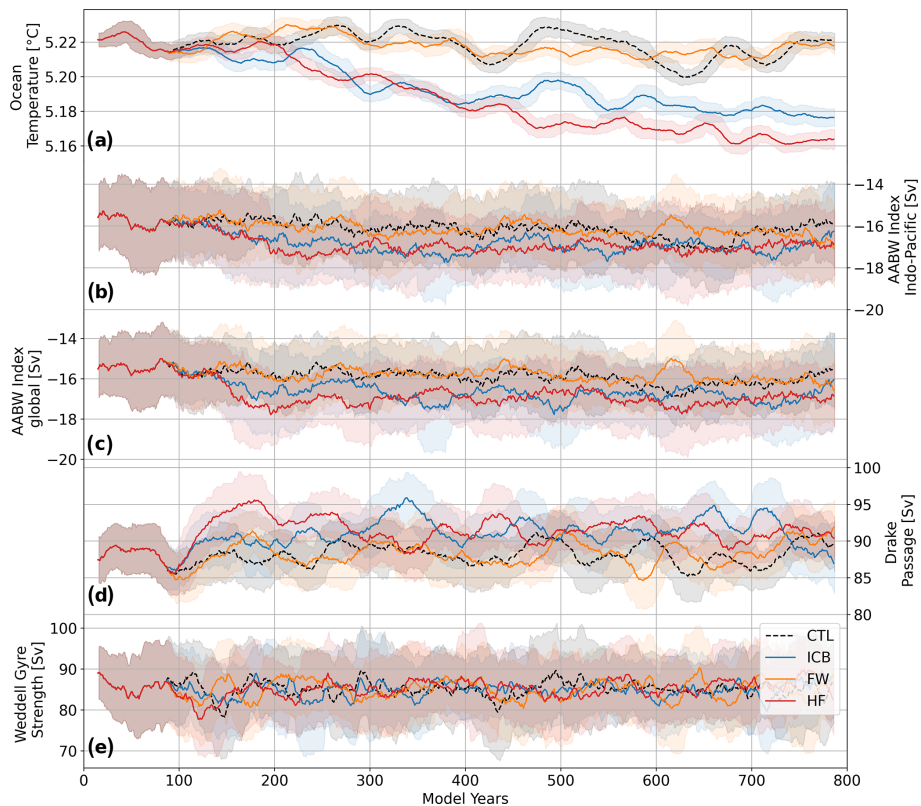


**Figure 8.** The 50-year rolling mean time series for global ocean mean temperature (a), Antarctic Bottom Water in the Indo-Pacific basin (b) and globally (c) as the maximum stream function value at 30° S, Drake Passage throughflow (d), and Weddell Gyre strength (e), defined as the difference between the maximum and the value at of the smallest closed contour line of the barotropic stream function, for ICB, ICB<sub>HF</sub>, ICB<sub>FW</sub>, and CTL; shaded areas indicate 1 standard deviation.

budget. The latent heat fluxes associated with iceberg melt even seem to play a dominant role in salinity changes up to intermediate depths and the formation of deep water (Figs. 6 and 7). Furthermore, they lead to surface cooling in the Weddell Sea (Fig. 4b and h), which is also found by Stern et al. (2016). The altered spatial freshwater distribution alone leads to a warming of large areas of the Southern Ocean's surface and subsurface waters (Fig. 4d) and thus buffers the cooling effect of iceberg melt. The iceberg-related heat fluxes are necessary to compensate for the surface warming and sustain the anomalous vertical heat transport.

A strengthening of AABW by up to 10% agrees well with findings by Jongma et al. (2009) and Martin and Adcroft (2010). ICB and ICB<sub>HF</sub> show similar strengthening of AABW in the Indo-Pacific basin and the most pronounced weakening of stratification in the Ross Shelf region, indicating the importance of the latent heat effect. Deep-water formation along continental shelves is a process commonly underestimated in CMIP6 models, whereas open-water deep convection is highly overestimated (Heuzé, 2021). A realistic representation of AABW formation along continental shelves is not feasible in our model setup due to spurious mixing along steep topography gradients. Our results aid in tackling the issue of open-ocean deep convection and emphasize the added value of a realistic representation of iceberg-related heat and freshwater fluxes in the Southern Ocean.

Our results indicate a cooling of deep-water masses in model runs with interactive icebergs. A pronounced cooling of the global deep ocean is recognized after around 200 years. The experiment that only considers heat fluxes from iceberg melting while using the default parameterized freshwater fluxes shows similar results as the fully coupled one including the iceberg-related meltwater. This result is not surprising as the same heat flux is applied to both simulations, leading to monotonous cooling. This cooling may aid in reducing deep-ocean temperature biases as found for FESOM2 (Streffing et al., 2022; Sidorenko et al., 2019) and other climate models (e.g., Delworth et al., 2006, 2012; Jungclaus et al., 2013; Rackow et al., 2019; Sterl et al., 2012) (compare Fig. 2). Including model icebergs in the Northern Hemisphere may lead to even enhanced cooling as the total global negative latent heat flux applied to the ocean would be larger than in our setup presented here. The effect of Northern Hemisphere icebergs on AABW and AMOC strength, however, may be more complex as the heat and freshwater fluxes due to iceberg melting affect the density profile differently, and the location of iceberg melt plays an important role.

## 5 Conclusions

We have studied the effect of interactive icebergs on the surface and in particular deep-ocean water mass changes. We used a fully coupled ESM with higher resolution (up

to  $\sim 1/3^\circ$ ) at continental shelf regions around Antarctica together with an interactive Lagrangian iceberg model (Rackow et al., 2017). The addition of the interactive iceberg model has a strong cooling impact at the surface (except in the Amundsen–Bellingshausen seas) in our study, which can act to decrease typical warm sea surface temperature biases in the Southern Ocean of climate models. This cooling combined with freshwater forcing could considerably delay Southern Ocean greenhouse warming in climate projections (Schloesser et al., 2019). This effect can be expected to increase with increasing iceberg discharge and an associated increase in latent heat flux due to iceberg melting. Furthermore, it might also play a role in explaining the observed lack of a multi-decadal decrease in Antarctic sea ice (Rackow et al., 2022). The region of the strongest warming after the inclusion of interactive icebergs (Amundsen–Bellingshausen seas) is in remarkable agreement with the location of the strongest observed warming around Antarctica. Therefore, our results could indicate a role for increased iceberg-related meltwater and heat fluxes in the observed warming. Interestingly, the addition of the iceberg model in our study leads to reduced deep-ocean temperatures in all ocean basins as well, where current climate models have been shown to typically be too warm (Rackow et al., 2019). Originating in the upper layers of the Southern Ocean, the cooling effect propagates northward. Our results suggest that the latent heat flux from iceberg melting is the main driver for this large-scale cooling. Furthermore, our results show an increased salinity on the continental shelves around Antarctica due to northward freshwater export by northward-drifting icebergs. This results in enhanced deep-water formation along continental shelves, which is a process commonly underestimated by CMIP6 models that do not include a sophisticated treatment of iceberg-related meltwater and heat fluxes. Our results thus emphasize the importance of realistically representing iceberg-related heat and freshwater fluxes in the high southern latitudes not only for surface-related biases but also in order to reduce long-standing biases in deep-water formation.

Icebergs play a crucial role in maintaining a suitable heat and freshwater balance in coupled climate models. Originating from glaciers or ice shelves, icebergs transport vast amounts of fresh water into the surrounding ocean. When they melt, this fresh water is released, significantly affecting the distribution of salinity and temperature in the ocean. Additionally, icebergs serve as a sink for heat. As they melt, they withdraw heat from the surrounding ocean, resulting in local cooling. These two effects, the freshwater input and the cooling, alter water density and consequently affect the vertical mixing of water masses and the stability of the water column. These changes have far-reaching consequences for the heat distribution within the ocean, with implications for regional and global climate patterns.

In the current generation of coupled climate models, icebergs are commonly not yet incorporated to simulate these



processes accurately, with a few exceptions; see, e.g., Smith et al. (2021). Including icebergs in ESMs enables a more accurate representation and feedbacks of ocean circulation patterns, the transport of heat, and the distribution of fresh water, contributing to improved understanding of past, present, and future climate change. The iceberg model aids in closing a gap between climate and ice sheet modeling. It allows for applications in a coupled climate–ice sheet model (like, for instance, used in Ackermann et al., 2020, or Niu et al., 2021), enabling the simulation of highly dynamic periods of abrupt climate change like Heinrich events. Icebergs will have a different impact on the global ocean circulation than coastal hosing in deglacial meltwater scenarios (Lohmann et al., 2020). It is therefore necessary to properly include interactive icebergs in climate models in order to examine relevant feedbacks. Applied in a bihemispheric setup, the model is an important tool in assessing teleconnections between the polar regions. Recent marine records from the Southern Ocean of iceberg-rafted debris provide a clear signal of ice sheet dynamics and variability (Weber et al., 2014). Adequate iceberg simulation will open a new avenue for interpreting deglacial meltwater and iceberg decay. Furthermore, the proposed enhanced configuration of AWI-ESM2.1 with reduced biases at the surface and in the deep ocean is a good candidate for better climate projections, as it includes a novel model component that can impact the timing of Southern Ocean greenhouse warming and Antarctic sea ice decline and thus ultimately projections of ice sheet retreat and global sea level rise.

### Appendix A: Size classes and scaling factors

The reference iceberg height  $h_{\text{ref}}$  for deriving the calving area flux  $A_{\text{tot}}$  from the calving volume flux  $V_{\text{tot}}$  is set to 250 m.

$$A_{\text{tot}} = V_{\text{tot}}/h_{\text{ref}} \quad (\text{A1})$$

The number of icebergs  $N$  is derived from the total calving area by subtracting with a reference iceberg area  $A_{\text{ref}}$ , here the median of the power-law distribution:

$$N = A_{\text{tot}}/A_{\text{ref}}, \quad (\text{A2})$$

with  $A_{\text{ref}} = 2^{1/(k-1)} x_{\text{min}}$ .

**Table A1.** Scaling factors for iceberg experiments performed in this study.

Area $A$ [km <sup>2</sup> ]	Scaling factor
$A \leq 0.1$	100
$0.1 < A \leq 1$	50
$1 < A \leq 10$	10
$10 < A \leq 100$	1
$A > 100$	1

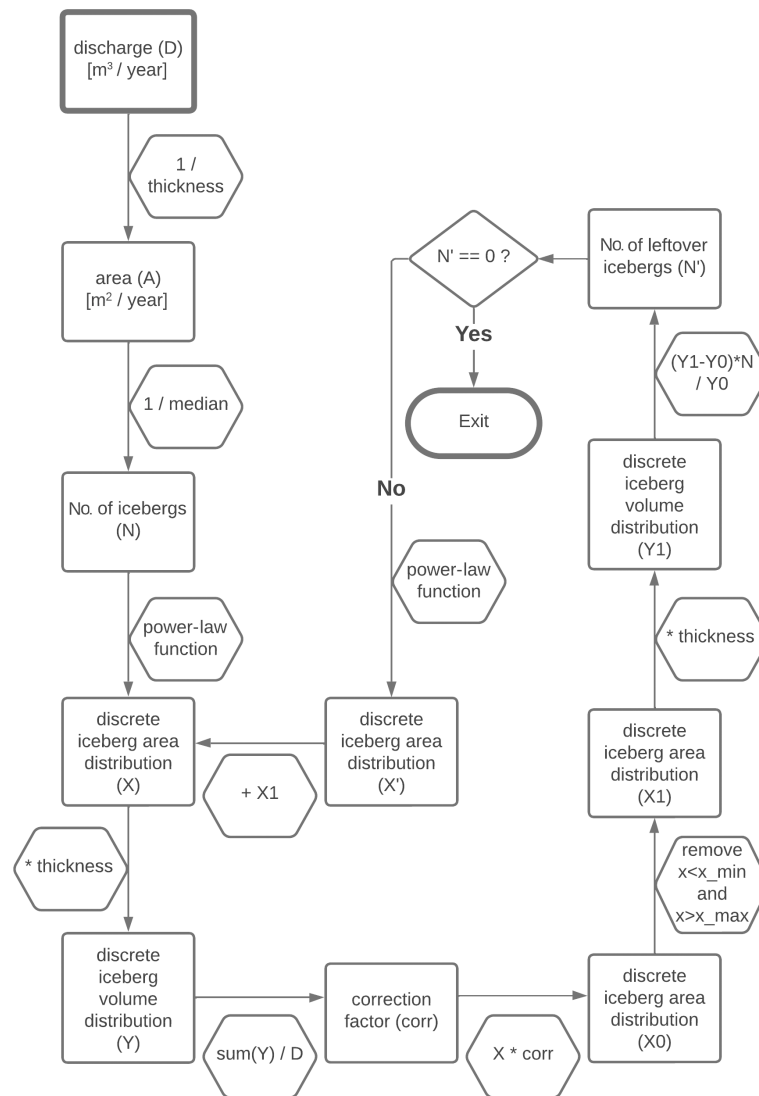


**Figure A1.** Scheme for the generation of discrete icebergs. The discharge field is integrated to receive a total discharge flux ( $D$ ), which is divided by a reference iceberg height of 250 m to receive an iceberg area flux ( $A$ ). A reference iceberg area size, here the median of the power-law distribution, is used to derive the number of icebergs to be generated ( $N$ ). The median is given by  $2^{1/(k-1)}x_{\min}$ , where  $k$  is  $-3/2$  and  $x_{\min}$  is  $0.01 \text{ km}^2$ . The number of icebergs  $N$  and the minimum area size  $x_{\min}$  are used with the Python power-law package to generate  $N$  discrete model icebergs with area size  $X$ . To compare the generated iceberg volume ( $Y$ ) with the prescribed total discharge,  $X$  is multiplied by the reference ice thickness and summed up to derive a scaling factor (corr).  $X$  is scaled with this factor to calculate a discrete area size distribution ( $X_0$ ) that is consistent with the prescribed total discharge. Those icebergs with areas smaller  $x_{\min}$  or larger  $x_{\max}$  are removed. For the total amount of removed iceberg volume, a new number of icebergs to be generated is calculated ( $N'$ ). If this is zero, no further model icebergs are needed; i.e., the calculated model icebergs sum up to the given total discharge. If  $N'$  does not equal zero, an iterative process is started, in which new model icebergs from a power-law distribution are generated until  $N'$  is zero.

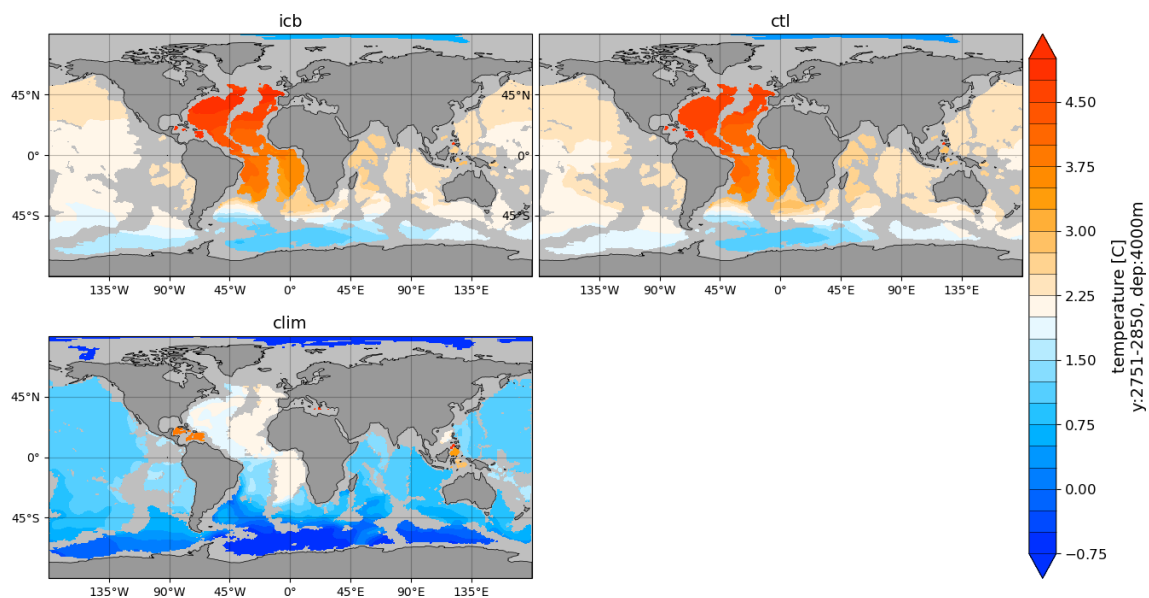


Figure A2. Temperature in 4000 m depth compared to PHC3.0 for the last 100 model years of CTL and ICB.

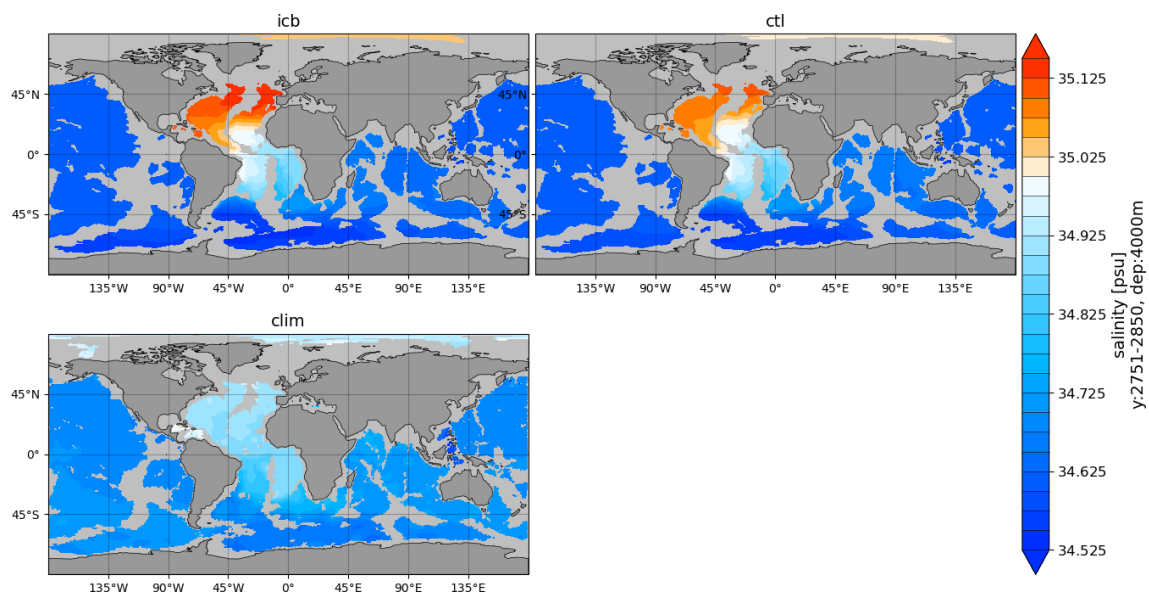
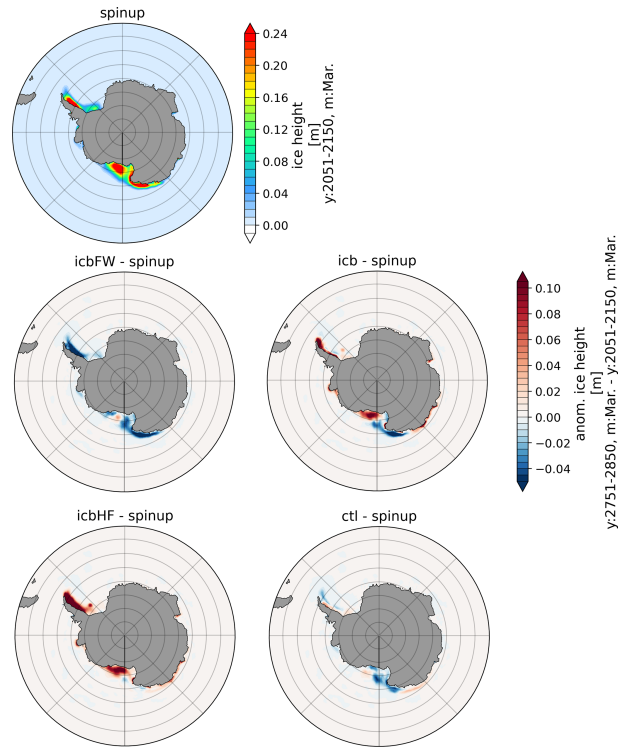
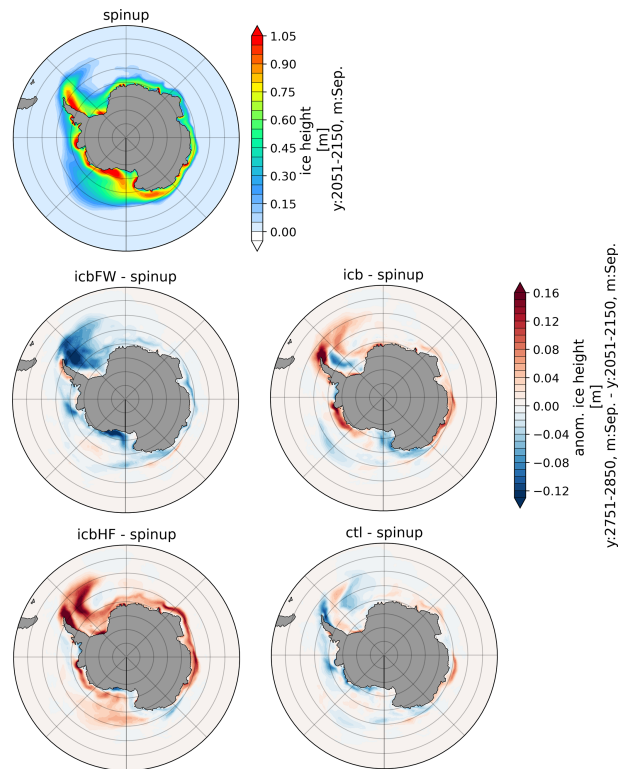


Figure A3. Salinity in 4000 m depth compared to PHC3.0 for the last 100 model years of CTL and ICB.



**Figure A4.** Anomaly of sea ice height for March of CTL, ICB<sub>HF</sub>, ICB<sub>FW</sub>, and ICB with respect to spin-up for the last 100 model years.



**Figure A5.** Anomaly of sea ice height for September of CTL, ICB<sub>HF</sub>, ICB<sub>FW</sub>, and ICB with respect to spin-up for the last 100 model years.

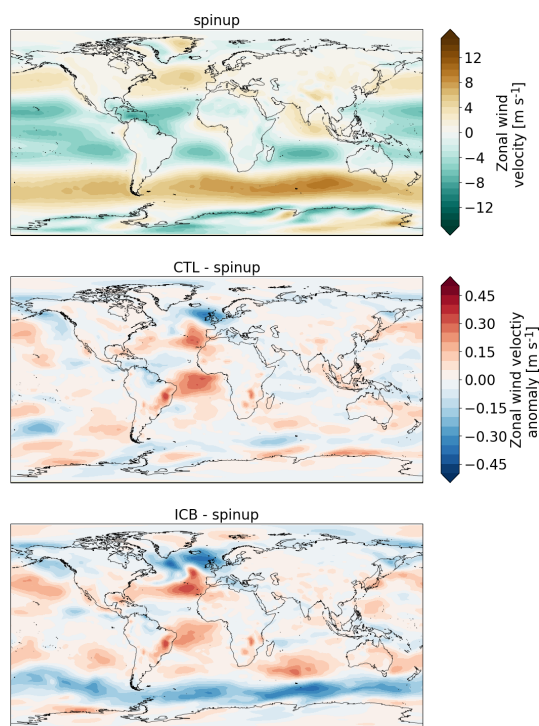


**Figure A6.** Zonal wind speed averaged over the last 100 model years for spin-up and zonal wind speed anomalies of CTL and ICB with respect to spin-up.

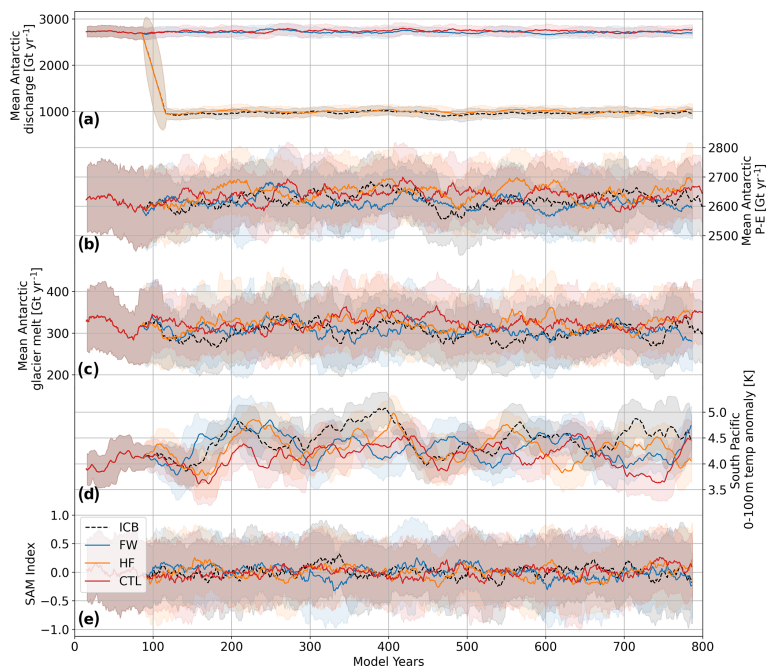


**Figure A7.** The 50-year running mean time series of (a) discharge from Antarctica into the ocean, (b) precipitation (including snowfall) minus evaporation over Antarctica, (c) glacier melt, (d) temperature averaged over the upper 100 m between 110–130° W and 55–65° S, and (e) SAM index calculated as the difference between the normalized monthly zonal sea level pressure at 40 and 65° S of CTL, ICB, ICB<sub>HF</sub> and ICB<sub>FW</sub>; shaded areas indicate 1 standard deviation.

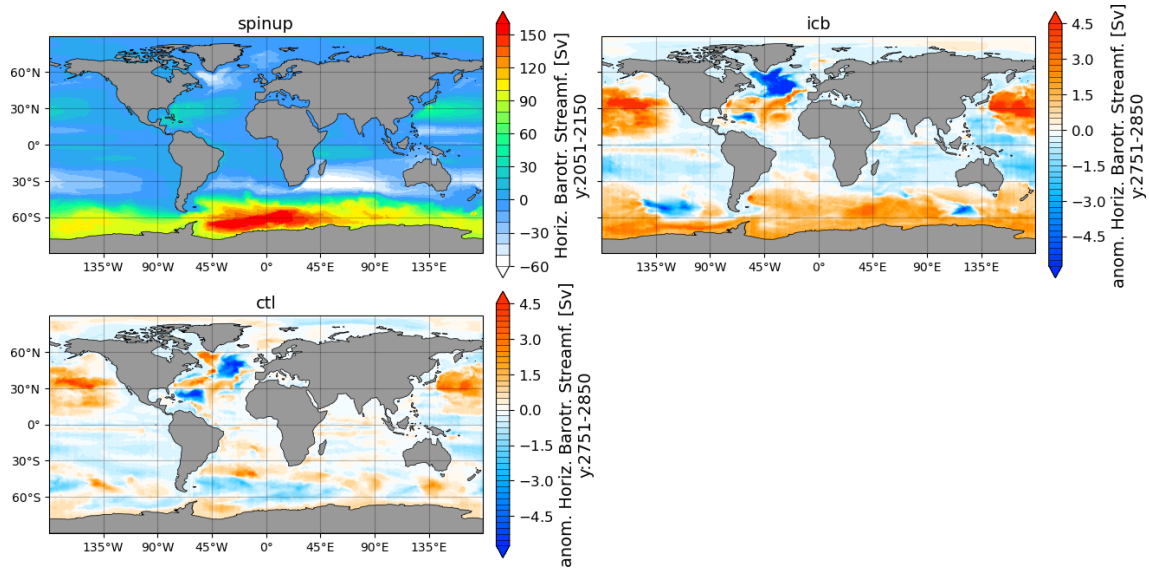


Figure A8. Barotropic stream function anomaly of CTL and ICB with respect to spin-up for the last 100 model years.

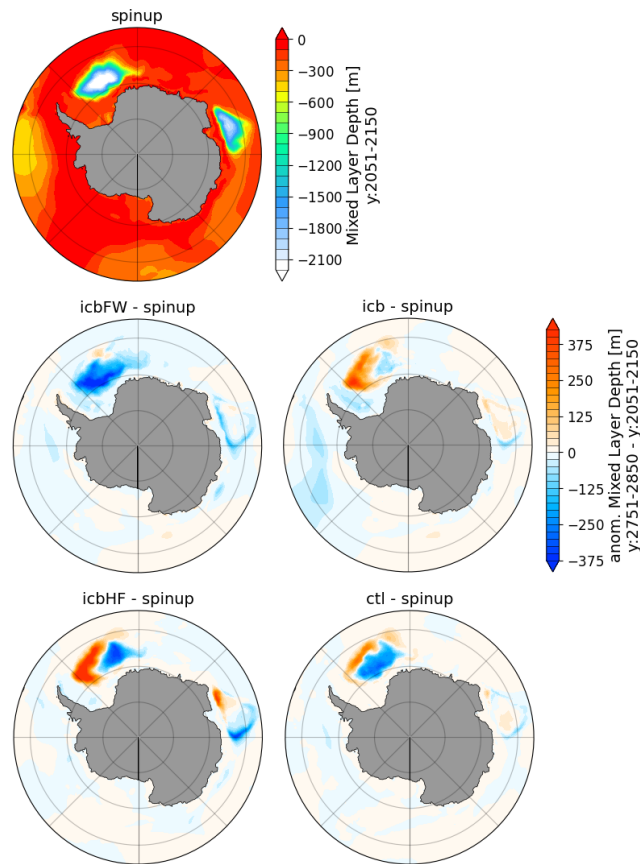
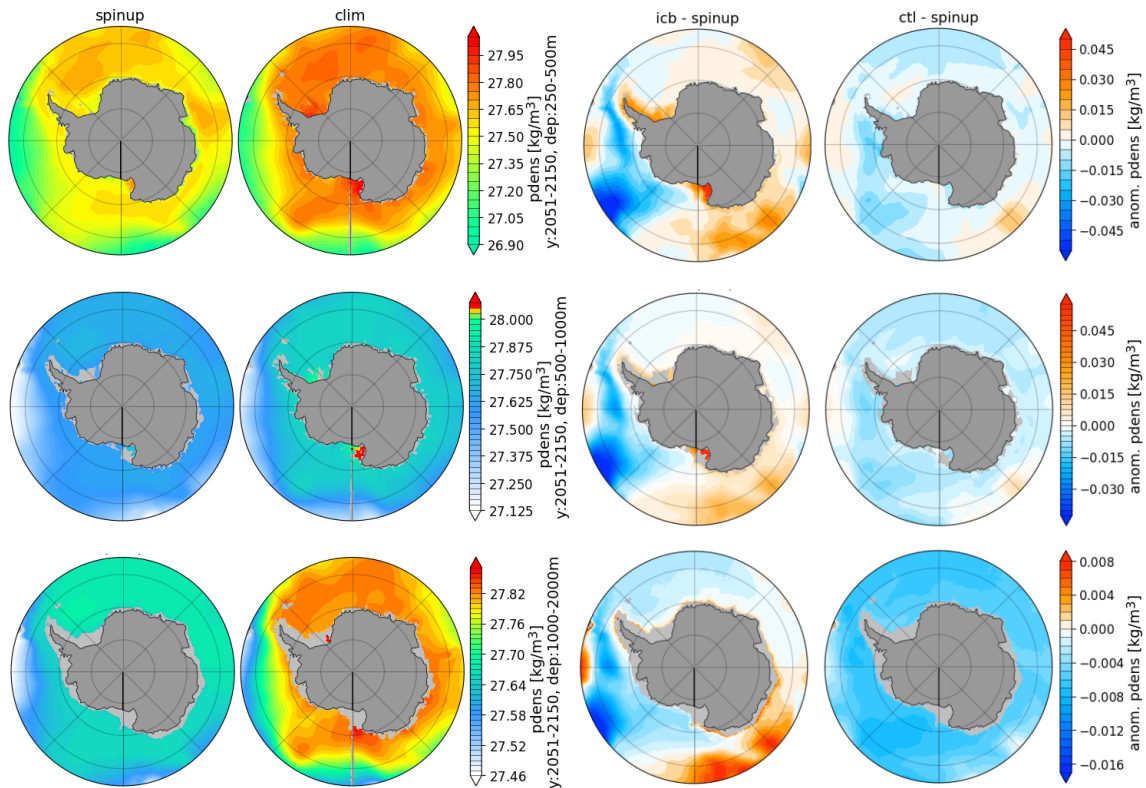


Figure A9. Mixed layer depth anomaly of CTL, ICB<sub>HF</sub>, ICB<sub>FW</sub>, and ICB with respect to spin-up for the last 100 model years.



**Figure A10.** Climatology and anomaly of potential density of CTL and ICB at 250–500, 500–1000, and 1000–2000 m with respect to spin-up for the last 100 model years.

## Appendix B: Estimation of heat budget

The global ocean cooling  $\Delta T$  due to latent heat fluxes from iceberg melting  $Q_1$  is estimated by

$$\Delta T = \frac{Q_1}{c_{p,\text{oce}} m_{\text{oce}}} \approx 0.01 \text{ K per century}, \quad (\text{B1})$$

with the heat capacity of seawater  $c_{p,\text{oce}} = 3850 \text{ J kg}^{-1} \text{ K}^{-1}$  and the global ocean mass  $m_{\text{oce}} = 1.4 \times 10^{21} \text{ kg}$ . The latent heat flux from iceberg melting is given by  $Q_1 = m_{\text{disch}} h_L$  with the total discharge flux  $m_{\text{disch}}$  of  $1731 \text{ Gt yr}^{-1}$  and the enthalpy of fusion of ice  $h_L$  with  $334 \text{ kJ kg}^{-1}$ .



*Code and data availability.* The ocean model FESOM2 source code is available on Zenodo at <https://doi.org/10.5281/zenodo.10000291> (Ackermann and Himstedt, 2023). The atmosphere model ECHAM6 is property of the Max Planck Institute for Meteorology. Its model code is available at [https://code.mpimet.mpg.de/login?back\\_url=https://Fcode.mpimet.mpg.de/projects/mpi-esm-users/files](https://code.mpimet.mpg.de/login?back_url=https://Fcode.mpimet.mpg.de/projects/mpi-esm-users/files) (last access: 18 January 2024) after registration at this site: <https://code.mpimet.mpg.de/projects/mpi-esm-license> (last access: 18 January 2023). The relevant changes that were used in this study are available on Zenodo at <https://doi.org/10.5281/zenodo.10009096> (Ackermann et al., 2023a). The `esm_tools` version used in this study is available at <https://doi.org/10.5281/zenodo.10018102> (Ackermann et al., 2023b).

All model output required to reproduce the figures can be found at <https://doi.org/10.5281/zenodo.10017868> (Ackermann, 2023a), <https://doi.org/10.5281/zenodo.10017840> (Ackermann, 2023b), <https://doi.org/10.5281/zenodo.10018019> (Ackermann, 2023c), <https://doi.org/10.5281/zenodo.10018131> (Ackermann, 2023d), and <https://doi.org/10.5281/zenodo.10018425> (Ackermann, 2023e). Scripts and input files required to recreate the simulations, as well as scripts for plotting, are available at <https://doi.org/10.5281/zenodo.10012787> (Ackermann, 2023f).

*Author contributions.* LA ported the iceberg model code from FESOM1 to AWIESM2, with support from TR and KH. LA coded the iceberg seeding routine, performed the simulations, and analyzed and visualized the results. All authors contributed to the paper and the discussion of the results.

*Competing interests.* The contact author has declared that none of the authors has any competing interests.

*Disclaimer.* Publisher's note: Copernicus Publications remains neutral with regard to jurisdictional claims made in the text, published maps, institutional affiliations, or any other geographical representation in this paper. While Copernicus Publications makes every effort to include appropriate place names, the final responsibility lies with the authors.

*Acknowledgements.* Thanks go to the Max Planck Institute in Hamburg (Germany) and colleagues from the Alfred Wegener Institute (AWI) for making ECHAM6-JSBACH and FESOM available to us. The simulations presented in this study are performed using the `esm_tools` (Barbi et al., 2021). Model simulations were performed on the high-performance computer “Levante” of the German Climate Computing Center (Deutsches Klimarechenzentrum, DKRZ). For the post-processing and plotting of FESOM data, the Python packages `pyfesom2` (<https://pyfesom2.readthedocs.io/en/latest/>, last access: 18 January 2024) and `tripyview` (<https://github.com/FESOM/tripyview>, last access: 18 January 2024) were used. We thank Robert Marsh and one anonymous reviewer for their constructive feedback and comments. The work was supported by the research topic “Ocean and Cryosphere under climate

change” in the program “Changing Earth – Sustaining our future” of the Helmholtz Society. Lars Ackermann acknowledges funding from the Federal Ministry for Education and Research initiative PalMod (project PalModII 1.3, BMBF grant no. 01LP1917A). Thomas Rackow acknowledges support from the European Commission's Horizon 2020 collaborative project NextGEMS (grant number 101003470).

*Financial support.* This research has been supported by the Federal Ministry for Education and Research initiative PalMod (project PalModII 1.3, BMBF grant no. 01LP1917A). Thomas Rackow received support from the European Commission's Horizon 2020 collaborative project NextGEMS (grant no. 101003470).

The article processing charges for this open-access publication were covered by the Alfred-Wegener-Institut Helmholtz-Zentrum für Polar- und Meeresforschung.

*Review statement.* This paper was edited by Alex Megann and reviewed by R. Marsh and one anonymous referee.

## References

- Ackermann, L.: LarsAckermann GMD Iceberg 2023 – model output CTL, Zenodo [data set], <https://doi.org/10.5281/zenodo.10017868>, 2023a.
- Ackermann, L.: LarsAckermann GMD Iceberg 2023 – model output ICB, Zenodo [data set], <https://doi.org/10.5281/zenodo.10017840>, 2023b.
- Ackermann, L.: LarsAckermann GMD Iceberg 2023 – model output ICBFW, Zenodo [data set], <https://doi.org/10.5281/zenodo.10018019>, 2023c.
- Ackermann, L.: LarsAckermann GMD Iceberg 2023 – model output ICBHF, Zenodo [data set], <https://doi.org/10.5281/zenodo.10018131>, 2023d.
- Ackermann, L.: LarsAckermann GMD Iceberg 2023 – model output SPINUP, Zenodo [data set], <https://doi.org/10.5281/zenodo.10018425>, 2023e.
- Ackermann, L.: LarsAckermann GMD Iceberg 2023 – model input and scripts, Zenodo [data set], <https://doi.org/10.5281/zenodo.10012787>, 2023f.
- Ackermann, L. and Himstedt, K.: FESOM2.1\_iceberg (2.1\_iceberg), Zenodo [code], <https://doi.org/10.5281/zenodo.10000291>, 2023.
- Ackermann, L., Danek, C., Gierz, P., and Lohmann, G.: AMOC Recovery in a Multicentennial Scenario Using a Coupled Atmosphere-Ocean-Ice Sheet Model, *Geophys. Res. Lett.*, 47, e2019GL086810, <https://doi.org/10.1029/2019GL086810>, 2020.
- Ackermann, L., Gierz, P., and Niu, L.: `echam_6.3.05p2` diff for AWI-ES2.1-iceberg, Zenodo [code], <https://doi.org/10.5281/zenodo.10009096>, 2023a.
- Ackermann, L., Andrés-Martínez, M., and Gierz, P.: `esm_tools` extension for AWI-ESM with FESOM2.1-iceberg (6.8.0\_iceberg), Zenodo [code], <https://doi.org/10.5281/zenodo.10018102>, 2023b.



- Barbat, M. M., Rackow, T., Hellmer, H. H., Wesche, C., and Mata, M. M.: Three years of near-coastal Antarctic iceberg distribution from a machine learning approach applied to SAR imagery, *J. Geophys. Res.-Oceans*, 124, 6658–6672, 2019.
- Barbi, D., Wieters, N., Gierz, P., Andrés-Martínez, M., Ural, D., Chegini, F., Khosravi, S., and Cristini, L.: ESM-Tools version 5.0: a modular infrastructure for stand-alone and coupled Earth system modelling (ESM), *Geosci. Model Dev.*, 14, 4051–4067, <https://doi.org/10.5194/gmd-14-4051-2021>, 2021.
- Bigg, G. R., Wadley, M. R., Stevens, D. P., and Johnson, J. A.: Prediction of iceberg trajectories for the North Atlantic and Arctic Oceans, *Geophys. Res. Lett.*, 23, 3587–3590, 1996.
- Bigg, G. R., Wadley, M. R., Stevens, D. P., and Johnson, J. A.: Modelling the dynamics and thermodynamics of icebergs, *Cold Reg. Sci. Technol.*, 26, 113–135, [https://doi.org/10.1016/S0165-232X\(97\)00012-8](https://doi.org/10.1016/S0165-232X(97)00012-8), 1997.
- Budge, J. S. and Long, D. G.: A Comprehensive Database for Antarctic Iceberg Tracking Using Scatterometer Data, *IEEE J. Sel. Top. Appl.*, 11, 434–442, <https://doi.org/10.1109/JSTARS.2017.2784186>, 2018.
- Bügelmayr, M., Roche, D. M., and Renssen, H.: How do icebergs affect the Greenland ice sheet under pre-industrial conditions? – a model study with a fully coupled ice-sheet–climate model, *The Cryosphere*, 9, 821–835, <https://doi.org/10.5194/tc-9-821-2015>, 2015.
- Claussen, M., Mysak, L., Weaver, A., Crucifix, M., Fichet, T., Loutre, M.-F., Weber, S., Alcamo, J., Alexeev, V., Berger, A., Calov, R., Ganopolski, A., Goosse, H., Lohmann, G., Lunkeit, F., Mokhov, I., Petoukhov, V., Stone, P., and Wang, Z.: Earth system models of intermediate complexity: closing the gap in the spectrum of climate system models, *Clim. Dynam.*, 18, 579–586, 2002.
- Danabasoglu, G., Yeager, S. G., Bailey, D., Behrens, E., Bentsen, M., Bi, D., Biastoch, A., Böning, C., Bozec, A., Canuto, V. M., Cassou, C., Chassignet, E., Coward, A. C., Danilov, S., Diansky, N., Drange, H., Farneti, R., Fernandez, E., Fogli, P. G., Forget, G., Fujii, Y., Griffies, S. M., Gusev, A., Heimbach, P., Howard, A., Jung, T., Kelley, M., Large, W. G., Leboissetier, A., Lu, J., Madec, G., Marsland, S. J., Masina, S., Navarra, A., Nurser, A. J. G., Pirani, A., Salas y Méliá, D., Samuels, B. L., Scheinert, M., Sidorenko, D., Treguier, A. M., Tsujino, H., Uotila, P., Valcke, S., Voldoire, A., and Wang, Q.: North Atlantic simulations in Coordinated Ocean-ice Reference Experiments phase II (CORE-II). Part II: Inter-annual to decadal variability, *Ocean Model.*, 97, 65–90, 2016.
- Danilov, S., Sidorenko, D., Wang, Q., and Jung, T.: The Finite-volume Sea ice–Ocean Model (FESOM2), *Geosci. Model Dev.*, 10, 765–789, <https://doi.org/10.5194/gmd-10-765-2017>, 2017.
- Delworth, T. L., Broccoli, A. J., Rosati, A., Stouffer, R. J., Balaji, V., Beesley, J. A., Cooke, W. F., Dixon, K. W., Dunne, J., Dunne, K. A., Durachta, J. W., Findell, K. L., Ginoux, P., Gnanadesikan, A., Gordon, C. T., Griffies, S. M., Gudgel, R., Harrison, M. J., Held, I. M., Hemler, R. S., Horowitz, L. W., Klein, S. A., Knutson, T. R., Kushner, P. J., Langenhorst, A. R., Lee, H. C., Lin, S. J., Lu, J., Malyshev, S. L., Milly, P. C. D., Ramaswamy, V., Russell, J., Schwarzkopf, M. D., Shevliakova, E., Sirutis, J. J., Spelman, M. J., Stern, W. F., Winton, M., Wittenberg, A. T., Wyman, B., Zeng, F., and Zhang, R.: GFDL’s CM2 global coupled climate models. Part I: Formulation and simulation characteristics, *J. Climate*, 19, 643–674, 2006.
- Delworth, T. L., Rosati, A., Anderson, W., Adcroft, A. J., Balaji, V., Benson, R., Dixon, K., Griffies, S. M., Lee, H.-C., Pacanowski, R. C., Vecchi, G. A., Wittenberg, A. T., Zeng, F., and Zhang, R.: Simulated Climate and Climate Change in the GFDL CM2.5 High-Resolution Coupled Climate Model, *J. Climate*, 25, 2755–2781, <https://doi.org/10.1175/JCLI-D-11-00316.1>, 2012.
- Depoorter, M. A., Bamber, J. L., Griggs, J. A., Lenaerts, J. T. M., Ligtenberg, S. R. M., van den Broeke, M. R., and Moholdt, G.: Calving fluxes and basal melt rates of Antarctic ice shelves, *Nature*, 502, 89–92, <https://doi.org/10.1038/nature12567>, 2013.
- Devilliers, M., Swingedouw, D., Mignot, J., Deshayes, J., Garric, G., and Ayache, M.: A realistic Greenland ice sheet and surrounding glaciers and ice caps melting in a coupled climate model, *Clim. Dynam.*, 57, 2467–2489, <https://doi.org/10.1007/s00382-021-05816-7>, 2021.
- Donohue, K., Tracey, K., Watts, D., Chidichimo, M. P., and Cherskin, T.: Mean antarctic circumpolar current transport measured in drake passage, *Geophys. Res. Lett.*, 43, 11–760, 2016.
- Dowdeswell, J. A., Whittington, R. J., and Hodgkins, R.: The sizes, frequencies, and freeboards of East Greenland icebergs observed using ship radar and sextant, *J. Geophys. Res.-Oceans*, 97, 3515–3528, 1992.
- Enderlin, E. M., Carrigan, C. J., Kochtitzky, W. H., Cuadros, A., Moon, T., and Hamilton, G. S.: Greenland iceberg melt variability from high-resolution satellite observations, *The Cryosphere*, 12, 565–575, <https://doi.org/10.5194/tc-12-565-2018>, 2018.
- England, M. R., Wagner, T. J., and Eisenman, I.: Modeling the breakup of tabular icebergs, *Science Advances*, 6, eabd1273, <https://doi.org/10.1126/sciadv.abd1273>, 2020.
- Gladstone, R. M., Bigg, G. R., and Nicholls, K. W.: Iceberg trajectory modeling and meltwater injection in the Southern Ocean, *J. Geophys. Res.-Oceans*, 106, 19903–19915, <https://doi.org/10.1029/2000JC000347>, 2001.
- Grosfeld, K., Schröder, M., Fahrbach, E., Gerdes, R., and Mackensen, A.: How iceberg calving and grounding change the circulation and hydrography in the Filchner Ice Shelf–Ocean System, *J. Geophys. Res.-Oceans*, 106, 9039–9055, <https://doi.org/10.1029/2000JC000601>, 2001.
- Hagemann, S. and Dümenil, L.: A parametrization of the lateral waterflow for the global scale, *Clim. Dynam.*, 14, 17–31, <https://doi.org/10.1007/s003820050205>, 1997.
- Hellmer, H. H. and Olbers, D. J.: A two-dimensional model for the thermohaline circulation under an ice shelf, *Antarctic Science*, 1, 325–336, 1989.
- Heuzé, C.: Antarctic Bottom Water and North Atlantic Deep Water in CMIP6 models, *Ocean Sci.*, 17, 59–90, <https://doi.org/10.5194/os-17-59-2021>, 2021.
- Holland, D. M. and Jenkins, A.: Modeling thermodynamic ice–ocean interactions at the base of an ice shelf, *J. Phys. Oceanogr.*, 29, 1787–1800, 1999.
- Jacobs, S. S., Helmer, H. H., Doake, C. S. M., Jenkins, A., and Frolich, R. M.: Melting of ice shelves and the mass balance of Antarctica, *J. Glaciol.*, 38, 375–387, <https://doi.org/10.3189/S0022143000002252>, 1992.
- Jongma, J. I., Driesschaert, E., Fichet, T., Goosse, H., and Renssen, H.: The effect of dynamic–thermodynamic icebergs on the Southern Ocean climate in a three-

- dimensional model, *Ocean Model.*, 26, 104–113, <https://doi.org/10.1016/j.ocemod.2008.09.007>, 2009.
- Jungclauss, J. H., Fischer, N., Haak, H., Lohmann, K., Marotzke, J., Matei, D., Mikolajewicz, U., Notz, D., and von Storch, J. S.: Characteristics of the ocean simulations in the Max Planck Institute Ocean Model (MPIOM) the ocean component of the MPI-Earth system model, *J. Adv. Model. Earth Sy.*, 5, 422–446, <https://doi.org/10.1002/jame.20023>, 2013.
- Koldunov, N. V., Aizinger, V., Rakowsky, N., Scholz, P., Sidorenko, D., Danilov, S., and Jung, T.: Scalability and some optimization of the Finite-volumE Sea ice–Ocean Model, Version 2.0 (FESOM2), *Geosci. Model Dev.*, 12, 3991–4012, <https://doi.org/10.5194/gmd-12-3991-2019>, 2019.
- Lohmann, G., Butzin, M., Eissner, N., Shi, X., and Stepanek, C.: Abrupt climate and weather changes across time scales, *Paleoceanography and Paleoclimatology*, 35, e2019PA003782, <https://doi.org/10.1029/2019PA003782>, 2020.
- Marsh, R., Ivchenko, V. O., Skliris, N., Alderson, S., Bigg, G. R., Madec, G., Blaker, A. T., Aksenov, Y., Sinha, B., Coward, A. C., Le Sommer, J., Merino, N., and Zalesny, V. B.: NEMO–ICB (v1.0): interactive icebergs in the NEMO ocean model globally configured at eddy-permitting resolution, *Geosci. Model Dev.*, 8, 1547–1562, <https://doi.org/10.5194/gmd-8-1547-2015>, 2015.
- Martin, M. A., Winkelmann, R., Haseloff, M., Albrecht, T., Bueler, E., Khroulev, C., and Levermann, A.: The Potsdam Parallel Ice Sheet Model (PISM-PIK) – Part 2: Dynamic equilibrium simulation of the Antarctic ice sheet, *The Cryosphere*, 5, 727–740, <https://doi.org/10.5194/tc-5-727-2011>, 2011.
- Martin, T. and Adcroft, A.: Parameterizing the fresh-water flux from land ice to ocean with interactive icebergs in a coupled climate model, *Ocean Model.*, 34, 111–124, <https://doi.org/10.1016/j.ocemod.2010.05.001>, 2010.
- Merino, N., Le Sommer, J., Durand, G., Jourdain, N. C., Madec, G., Mathiot, P., and Tournadre, J.: Antarctic icebergs melt over the Southern Ocean: Climatology and impact on sea ice, *Ocean Model.*, 104, 99–110, <https://doi.org/10.1016/j.ocemod.2016.05.001>, 2016.
- Niu, L., Lohmann, G., Gierz, P., Gowan, E. J., and Knorr, G.: Coupled climate-ice sheet modelling of MIS-13 reveals a sensitive Cordilleran Ice Sheet, *Global Planet. Change*, 200, 103474, <https://doi.org/10.1016/j.gloplacha.2021.103474>, 2021.
- Orsi, A. H., Whitworth III, T., and Nowlin Jr., W. D.: On the meridional extent and fronts of the Antarctic Circumpolar Current, *Deep-Sea Res. Pt. I*, 42, 641–673, 1995.
- Qi, M., Liu, Y., Liu, J., Cheng, X., Lin, Y., Feng, Q., Shen, Q., and Yu, Z.: A 15-year circum-Antarctic iceberg calving dataset derived from continuous satellite observations, *Earth Syst. Sci. Data*, 13, 4583–4601, <https://doi.org/10.5194/essd-13-4583-2021>, 2021.
- Rackow, T.: Modellierung der Eisbergdrift als Erweiterung eines Finite-Elemente-Meeris-Ozean-Modells, Diplom thesis, Universität Bremen, Alfred-Wegener-Institut für Polar- und Meeresforschung, <https://epic.awi.de/id/eprint/26128/> (last access: 18 January 2024), 2011.
- Rackow, T., Wesche, C., Timmermann, R., Hellmer, H. H., Juricke, S., and Jung, T.: A simulation of small to giant Antarctic iceberg evolution: Differential impact on climatology estimates, *J. Geophys. Res.-Oceans*, 122, 3170–3190, <https://doi.org/10.1002/2016JC012513>, 2017.
- Rackow, T., Goessling, H. F., Jung, T., Sidorenko, D., Semmler, T., Barbi, D., and Handorf, D.: Towards multi-resolution global climate modeling with ECHAM6-FESOM. Part II: climate variability, *Clim. Dynam.*, 50, <https://doi.org/10.1007/s00382-016-3192-6>, 2018.
- Rackow, T., Sein, D. V., Semmler, T., Danilov, S., Koldunov, N. V., Sidorenko, D., Wang, Q., and Jung, T.: Sensitivity of deep ocean biases to horizontal resolution in prototype CMIP6 simulations with AWI-CM1.0, *Geosci. Model Dev.*, 12, 2635–2656, <https://doi.org/10.5194/gmd-12-2635-2019>, 2019.
- Rackow, T., Danilov, S., Goessling, H. F., Hellmer, H. H., Sein, D. V., Semmler, T., Sidorenko, D., and Jung, T.: Delayed Antarctic sea-ice decline in high-resolution climate change simulations, *Nat. Commun.*, 13, 637, <https://doi.org/10.1038/s41467-022-28259-y>, 2022.
- Reick, C. H., Raddatz, T., Brovkin, V., and Gayler, V.: Representation of natural and anthropogenic land cover change in MPI-ESM, *J. Adv. Model. Earth Sy.*, 5, 459–482, <https://doi.org/10.1002/jame.20022>, 2013.
- Reick, C. H., Gayler, V., Goll, D., Hagemann, S., Heidkamp, M., Nabel, J. E., Raddatz, T., Roeckner, E., Schnur, R., and Wilkenskeld, S.: JSBACH 3 – The land component of the MPI Earth System Model: documentation of version 3.2, [https://pure.mpg.de/rest/items/item\\_3279802\\_26/component/file\\_3316522/content](https://pure.mpg.de/rest/items/item_3279802_26/component/file_3316522/content) (last access: 18 January 2024), 2021.
- Schloesser, F., Friedrich, T., Timmermann, A., DeConto, R. M., and Pollard, D.: Antarctic iceberg impacts on future Southern Hemisphere climate, *Nat. Clim. Change*, 9, 672–677, <https://doi.org/10.1038/s41558-019-0546-1>, 2019.
- Scholz, P., Sidorenko, D., Gurses, O., Danilov, S., Koldunov, N., Wang, Q., Sein, D., Smolentseva, M., Rakowsky, N., and Jung, T.: Assessment of the Finite-volumE Sea ice–Ocean Model (FESOM2.0) – Part 1: Description of selected key model elements and comparison to its predecessor version, *Geosci. Model Dev.*, 12, 4875–4899, <https://doi.org/10.5194/gmd-12-4875-2019>, 2019.
- Scholz, P., Sidorenko, D., Danilov, S., Wang, Q., Koldunov, N., Sein, D., and Jung, T.: Assessment of the Finite-VolumE Sea ice–Ocean Model (FESOM2.0) – Part 2: Partial bottom cells, embedded sea ice and vertical mixing library CVMix, *Geosci. Model Dev.*, 15, 335–363, <https://doi.org/10.5194/gmd-15-335-2022>, 2022.
- Sein, D. V., Danilov, S., Biastoch, A., Durgadoo, J. V., Sidorenko, D., Harig, S., and Wang, Q.: Designing variable ocean model resolution based on the observed ocean variability, *J. Adv. Model. Earth Sy.*, 8, 904–916, 2016.
- Siahaan, A., Smith, R. S., Holland, P. R., Jenkins, A., Gregory, J. M., Lee, V., Mathiot, P., Payne, A. J., Ridley, J. K., and Jones, C. G.: The Antarctic contribution to 21st-century sea-level rise predicted by the UK Earth System Model with an interactive ice sheet, *The Cryosphere*, 16, 4053–4086, <https://doi.org/10.5194/tc-16-4053-2022>, 2022.
- Sidorenko, D., Rackow, T., Jung, T., Semmler, T., Barbi, D., Danilov, S., Dethloff, K., Dorn, W., Fieg, K., Gößling, H. F., Handorf, D., Harig, S., Hiller, W., Juricke, S., Losch, M., Schröter, J., Sein, D., and Wang, Q.: Towards multi-resolution global climate modeling with ECHAM6–FESOM. Part I: model

- formulation and mean climate, *Clim. Dynam.*, 44, 757–780, <https://doi.org/10.1007/s00382-014-2290-6>, 2015.
- Sidorenko, D., Goessling, H., Koldunov, N., Scholz, P., Danilov, S., Barbi, D., Cabos, W., Gurses, O., Harig, S., Hinrichs, C., Juricke, S., Lohmann, G., Losch, M., Mu, L., Rackow, T., Rakowsky, N., Sein, D., Semmler, T., Shi, X., Stepanek, C., Streffing, J., Wang, Q., Wekerle, C., Yang, H., and Jung, T.: Evaluation of FESOM2.0 Coupled to ECHAM6.3: Preindustrial and High-ResMIP Simulations, *J. Adv. Model. Earth Sy.*, 11, 3794–3815, <https://doi.org/10.1029/2019MS001696>, 2019.
- Smith, R. S., Mathiot, P., Siahann, A., Lee, V., Cornford, S. L., Gregory, J. M., Payne, A. J., Jenkins, A., Holland, P. R., Riddle, J. K., and Jones C. G.: Coupling the U.K. Earth System Model to dynamic models of the Greenland and Antarctic ice sheets, *J. Adv. Model. Earth Sy.*, 13, e2021MS002520, <https://doi.org/10.1029/2021MS002520>, 2021.
- Steele, M., Morley, R., and Ermold, W.: PHC: A global ocean hydrography with a high-quality Arctic Ocean, *J. Climate*, 14, 2079–2087, 2001.
- Sterl, A., Bintanja, R., Brodeau, L., Gleeson, E., Koenigk, T., Schmith, T., Semmler, T., Severijns, C., Wyser, K., and Yang, S.: A look at the ocean in the EC-Earth climate model, *Clim. Dynam.*, 39, 2631–2657, <https://doi.org/10.1007/s00382-011-1239-2>, 2012.
- Stern, A. A., Johnson, E., Holland, D. M., Wagner, T. J., Wadhams, P., Bates, R., Abrahamsen, E. P., Nicholls, K. W., Crawford, A., Gagnon, J., and Tremblay, J.-E.: Wind-driven upwelling around grounded tabular icebergs, *J. Geophys. Res.-Oceans*, 120, 5820–5835, <https://doi.org/10.1002/2015JC010805>, 2015.
- Stern, A. A., Adcroft, A., and Sergienko, O.: The effects of Antarctic iceberg calving-size distribution in a global climate model, *J. Geophys. Res.-Oceans*, 121, 5773–5788, <https://doi.org/10.1002/2016JC011835>, 2016.
- Stevens, B., Giorgetta, M., Esch, M., Mauritsen, T., Crueger, T., Rast, S., Salzmann, M., Schmidt, H., Bader, J., Block, K., Brokopf, R., Fast, I., Kinne, S., Kornblueh, L., Lohmann, U., Pincus, R., Reichler, T., and Roeckner, E.: Atmospheric component of the MPI-M Earth System Model: ECHAM6, *J. Adv. Model. Earth Sy.*, 5, 146–172, <https://doi.org/10.1002/jame.20015>, 2013.
- Streffing, J., Sidorenko, D., Semmler, T., Zampieri, L., Scholz, P., Andrés-Martínez, M., Koldunov, N., Rackow, T., Kjellsson, J., Goessling, H., Athanase, M., Wang, Q., Hegewald, J., Sein, D. V., Mu, L., Fladrich, U., Barbi, D., Gierz, P., Danilov, S., Juricke, S., Lohmann, G., and Jung, T.: AWI-CM3 coupled climate model: description and evaluation experiments for a prototype post-CMIP6 model, *Geosci. Model Dev.*, 15, 6399–6427, <https://doi.org/10.5194/gmd-15-6399-2022>, 2022.
- Stuart, K. M. and Long, D. G.: Tracking large tabular icebergs using the SeaWinds Ku-band microwave scatterometer, *Deep-Sea Res. Pt. II*, 58, 1285–1300, <https://doi.org/10.1016/j.dsr2.2010.11.004>, 2011.
- Tournadre, J., Bouhier, N., Girard-Ardhuin, F., and Rémy, F.: Antarctic icebergs distributions 1992–2014, *J. Geophys. Res.-Oceans*, 121, 327–349, <https://doi.org/10.1002/2015JC011178>, 2016.
- Wang, Q., Danilov, S., Sidorenko, D., Timmermann, R., Wekerle, C., Wang, X., Jung, T., and Schröter, J.: The Finite Element Sea Ice-Ocean Model (FESOM) v.1.4: formulation of an ocean general circulation model, *Geosci. Model Dev.*, 7, 663–693, <https://doi.org/10.5194/gmd-7-663-2014>, 2014.
- Wang, Q., Ilicak, M., Gerdes, R., Drange, H., Aksenov, Y., Bailey, D. A., Bentsen, M., Biastoch, A., Bozec, A., Böning, C., Cassou, C., Chassignet, E., Coward, A. C., Curry, B., Danabasoglu, G., Danilov, S., Fernandez, E., Fogli, P. G., Fujii, Y., Griffies, S. M., Iovino, D., Jahn, A., Jung, T., Large, W. G., Lee, C., Lique, C., Lu, J., Masina, S., Nurser, A. J. G., Rabe, B., Roth, C., Salas y Mélia, D., Samuels, B. L., Spence, P., Tsujino, H., Valcke, S., Voldoire, A., Wang, X., and Yeager, S. G.: An assessment of the Arctic Ocean in a suite of interannual CORE-II simulations. Part I: Sea ice and solid freshwater, *Ocean Model.*, 99, 110–132, 2016a.
- Wang, Q., Ilicak, M., Gerdes, R., Drange, H., Aksenov, Y., Bailey, D. A., Bentsen, M., Biastoch, A., Bozec, A., Böning, C., Cassou, C., Chassignet, E., Coward, A. C., Curry, B., Danabasoglu, G., Danilov, S., Fernandez, E., Fogli, P. G., Fujii, Y., Griffies, S. M., Iovino, D., Jahn, A., Jung, T., Large, W. G., Lee, C., Lique, C., Lu, J., Masina, S., Nurser, A. J. G., Rabe, B., Roth, C., Salas y Mélia, D., Samuels, B. L., Spence, P., Tsujino, H., Valcke, S., Voldoire, A., Wang, X., and Yeager, S. G.: An assessment of the Arctic Ocean in a suite of interannual CORE-II simulations. Part II: Liquid freshwater, *Ocean Model.*, 99, 86–109, 2016b.
- Weber, M., Clark, P., Kuhn, G., Timmermann, A., Spreng, D., Gladstone, R., Zhang, X., Lohmann, G., Menviel, L., Chikamoto, M., Friedrich, T., and Ohlwein, C.: Millennial-scale variability in Antarctic ice-sheet discharge during the last deglaciation, *Nature*, 510, 134–138, 2014.
- Whitworth, T. and Peterson, R.: Volume transport of the Antarctic Circumpolar Current from bottom pressure measurements, *J. Phys. Oceanogr.*, 15, 810–816, 1985.
- Winkelmann, R., Martin, M. A., Haseloff, M., Albrecht, T., Bueler, E., Khroulev, C., and Levermann, A.: The Potsdam Parallel Ice Sheet Model (PISM-PIK) – Part I: Model description, *The Cryosphere*, 5, 715–726, <https://doi.org/10.5194/tc-5-715-2011>, 2011.